AD A059049

LEVEL II
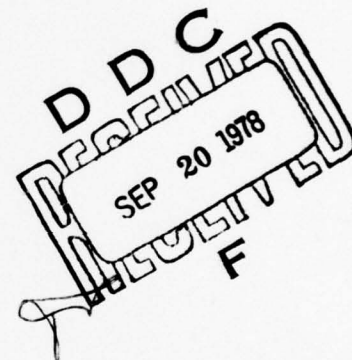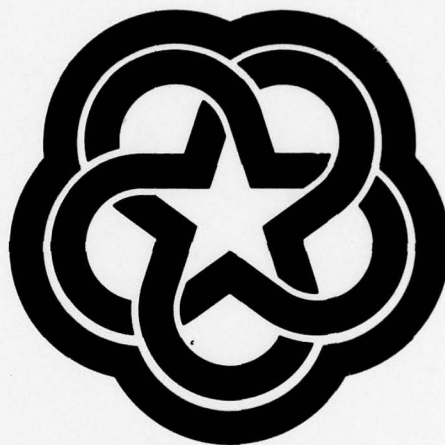
AFOSR-TR- 78-1243

PLASMA-LASER INTERACTIONS WITH SOLID POLYSTYRENE MICROSPHERES

by

David L. Smith

LEVEL II

D D C
SEP 20 1978
F

October 3, 1977

PLASMA LABORATORY
DEPARTMENT OF ELECTRICAL ENGINEERING

TEXAS TECH UNIVERSITY

Lubbock, Texas 79409

78 09 05 069

1. REPORT NUMBER	2. GOVT ACCESSION NO.	3. RECIPIENT'S CATALOG NUMBER
AFOSR-TR- 78-1243		

4. TITLE (and Subtitle)	5. TYPE OF REPORT & PERIOD COVERED
PLASMA-LASER INTERACTIONS WITH SOLID POLYSTYRENE MICROSPHERES	Interim
	6. PERFORMING ORG. REPORT NUMBER

7. AUTHOR(s)	8. CONTRACT OR GRANT NUMBER(s)
David L. Smith	AFOSR 74-2639

9. PERFORMING ORGANIZATION NAME AND ADDRESS	10. PROGRAM ELEMENT, PROJECT, TASK AREA & WORK UNIT NUMBERS
Plasma Laboratory Dept. of Elec. Engr. Texas Tech University Lubbock, Texas 79409	61102 F 23 01/A2

11. CONTROLLING OFFICE NAME AND ADDRESS	12. REPORT DATE
AFOSR/NP Bolling Air Force Base Washington, D.C. 20332	October 3, 1977
	13. NUMBER OF PAGES
	96

14. MONITORING AGENCY NAME & ADDRESS(if different from Controlling Office)	15. SECURITY CLASS. (of this report)
	Unclassified
	15a. DECLASSIFICATION/DOWNGRADING SCHEDULE

16. DISTRIBUTION STATEMENT (of this Report)

Approved for public release;
distribution unlimited.

17. DISTRIBUTION STATEMENT (of the abstract entered in Block 20, if different from Report)

18. SUPPLEMENTARY NOTES

19. KEY WORDS (Continue on reverse side if necessary and identify by block number)

Plasma	Ablation
Plasma-Solid Interaction	Pellet
Laser	Pellet-Plasma-Laser Interaction

micrometers

20. ABSTRACT (Continue on reverse side if necessary and identify by block number)

The basic mechanisms involved in a solid-plasma interaction have been studied. In order to measure the ablation rates of solid polystyrene spheres of 50 to 150 μm radii, the pellets were suspended on glass fibers and exposed to a dense $(n_e \approx 5 \times 10^{22} m^{-3})$, hot $(T_e < T_i \approx 120 eV)$ theta pinch plasma. The pellet sizes were measured before and after each 2 μs

microsec → next pag

DD 1 JAN 73 FORM 1473   EDITION OF 1 NOV 65 IS OBSOLETE

pellet-plasma interaction, and the results were plotted against several plasma parameters. Qualitative agreement with recent theoretical scaling laws was obtained. The pellet surfaces acquired a fine polish when exposed to a plasma as indicated by electron microscopy. Comparison of the ionization intensities in the ablating neutral material through the first four carbon lines indicated pellet cloud temperatures in the range of 5 eV. Both spectroscopy and streak camera photography showed that focusing a Q-switched ruby laser on the pellet during the plasma interaction produced a marked increase in the ionization intensities that was sustained long after the laser pulse. The pellet-plasma interaction alone was determined to be an inefficient means of generating X-rays. The combination pellet-plasma-laser interaction promises to be a feasible radiation source for durations much longer than those produced with only the laser-solid system.

PLASMA-LASER INTERACTIONS WITH SOLID

POLYSTYRENE MICROSPHERES.

by

David L. Smith

3 October, 1977

Interim Technical Report No. 7 on

Grant AFOSR-74-2639

"Dense Plasma Heating and Radiation Generation"

AFOSR-74-2639

Principal Investigator: M. Kristiansen, Horn Professor
Co-Principal Investigator: M.O. Hagler, Professor

Plasma Laboratory
Department of Electrical Engineering
Texas Tech University
Lubbock, Texas 79409

AFOSRI TR-78-1243

ABSTRACT

The basic mechanisms involved in a solid-plasma in-
teraction have been studied. In order to measure the
ablation rates of solid polystyrene spheres of 50 to 150
μm radii, the pellets were suspended on glass fibers and
exposed to a dense ($n_e \doteq 5 \times 10^{22}$ m^{-3}), hot ($T_e < T_i \doteq$
120 eV) theta pinch plasma. The pellet sizes were mea-
sured before and after each 2 μs pellet-plasma interac-
tion, and the results were plotted against several plasma
parameters. Qualitative agreement with recent theoretical
scaling laws was obtained. The pellet surfaces acquired
a fine polish when exposed to a plasma as indicated by
electron microscopy. Comparison of the ionization inten-
sities in the ablating neutral material through the first
four carbon lines indicated pellet cloud temperatures in
the range of 5 eV. Both spectroscopy and streak camera
photography showed that focusing a Q-switched ruby laser
on the pellet during the plasma interaction produced a
marked increase in the ionization intensities that was
sustained long after the laser pulse. The pellet-plasma
interaction alone was determined to be an inefficient
means of generating X-rays. The combination pellet-

plasma-laser interaction promises to be a feasible

radiation source for durations much longer than those

produced with only the laser-solid system.

ACKNOWLEDGEMENTS

TABLE OF CONTENTS

LIST OF FIGURES

LIST OF SYMBOLS AND UNITS

Symbol	Definition	MKS Units
d	Plasma thickness	m
e	Electron charge	C
k	Boltzmann's constant	J/°K
ℓ_{ab}	Laser power absorption length	m
m_e	Electron mass	kg
n	Empirical constant	
n_e	Electron density	m^{-3}
$\bar{n}_e$	Average electron density during interaction	m^{-3}
n_i	Ion density	m^{-3}
r_p	Instantaneous pellet radius	m
$\dot{r}_p$	Pellet surface regression speed	m/s
r_{po}	Initial pellet radius	m
t	Time	s
v	Fluid velocity	m/s
x	Linear spatial coordinate	m
B	Magnetic flux density	T
C_ℓ	Specific heat of a liquid	J/kg-°K
C_s	Specific heat of a solid	J/kg-°K
E	Energy	J

Symbol	Definition	MKS Units
E_{ff}	Transmitted bremsstrahlung energy	J
F_e	Plasma energy flux (power density)	W/m^2
H_2	Hydrogen molecule	
I	Local laser intensity	W/m^2
I_o	Initial laser intensity	W/m^2
K	Proportionality constant	
$L(E)$	Energy dependent loss function	$J-m^2$
L_m	Latent heat of melting	J/kg
L_v	Latent heat of vaporization	J/kg
M	Ion mass	kg
P_o	Initial filling pressure	mTorr
T_e	Electron temperature	$°K$
$\overline{T}_e$	Average electron temperature during interaction	$°K$
T_i	Ion temperature	$°K$
T_m	Melting temperature	$°K$
T_v	Vaporization temperature	$°K$
U_s	Surface regression speed of a flat target	m/s
V	Plasma volume	m^3
Z	Atomic number	
$\overline{Z^*}$	Mean effective ion charge	C
α	Transmission coefficient	
γ	Effective energy flux cross section	m^2
ε_o	Permittivity constant	F/m

Symbol	Definition	MKS Units
ν_o	Laser frequency	Hz
ν_p	Plasma frequency	Hz
σ	Stefan-Boltzmann constant	$W/m^2 - °K^4$
ρ_s	Density of a solid	kg/m^3
τ_h	Characteristic hydrodynamic expansion or contraction time	s
τ_o	Laser duration or pulsewidth	s
τ_p	Plasma duration	s
Δr_p	Measured reduction of a pellet's radius	m
Δt	Pellet-plasma interaction time	s
$\Lambda(\nu_o)$	Ratio of Debye length to impact parameter calculated with ν_o	

CHAPTER I

INTRODUCTION

Sequential interactions of solid pellets with hot plasmas and lasers of various wavelengths may lead to efficient generation of large X-ray fluxes of interest for various applications. Also, the concept of refueling thermonuclear reactors by high-speed pellet injection is of interest because of the small amount of injection energy that is required as opposed to other refueling methods. Applications of this technique demand an understanding of how the pellet is vaporized and ionized as it enters a plasma environment. Practical economic and physics considerations then allow the determination of the required initial pellet sizes and/or velocities. Other apparent applications for the laser-plasma-pellet interaction include the development of plasma diagnostic techniques and an evaluation of the fusion torch concept.[1] Finally, the pellet cloud could be formed or shaped by laser beams in order to tailor the density distribution in a fusion device. As an extension of an earlier study by Nunnally[2] this work had the combined purposes of actually measuring the ablation rates of solid polysty-

1

rene, $(C_6H_5-CH{=}CH_2) \cdot n$, microspheres that were exposed to a theta pinch plasma and various laser pulses and also to determine the feasibility of developing this technique into an efficient X-ray source.

Polystyrene pellets were used because of their availability and relative ease of handling. Serious investigations are being conducted into the use of low average atomic number polymer spherical microshells as the fuel "envelopes" for the laser fusion scheme because they are stable and easy to fabricate.[3,4] Among the possible candidates are polymethylmacrolate, polyvinyl alcohol, and polystyrene, which increases the interest in laser and plasma interaction with this material.

To meet the goals of this research and to lend support to some of the recently developed theories described in Chapter II, a hot plasma environment for the solid pellets was generated by the TeePee 1B theta pinch system that is discussed in Chapter III. This theta pinch produced the large energy flux of a fusion reactor ($\doteq 10^{13}$ W/m^2), but the thermal conductivity was considerably less than that desired. Suspending a pellet of about 200 μm diameter on a fine glass fiber enabled reproducible interactions to be observed with the plasma, a ruby laser, a CO_2 laser, and certain combinations of plasma and laser interactions. The laser-plasma inter-

actions with the pellets were investigated with image
converter photography, limited spectroscopy, and Mach
Zehnder interferometry to compare properties of this
radiation generation system to the interactions involving
the plasma alone. For the cases without the laser, the
pellets were usually retrievable and the change in size
could be directly measured. Analysis of the retrieved
pellets produced qualitative agreement with the theoret-
ical scaling laws.

The previous experiments[5] disproved earlier
theories[6-10] which indicate that a 5×10^{22} m^{-3}, 300 eV
plasma of about 1 µsec duration has sufficient energy
flux and thermal conductivity to vaporize and ionize a
substantial fraction of a 200 µm polystyrene pellet. In
the present experiment only very small changes in the
pellet radii were observed. Almost all the fiber that
was exposed to the hot plasma was, however, either
vaporized or broken up into a fine residue. Since the
mean free paths for the electron-neutral and ion-neutral
collisions were on the order of the pellet's $\pm$ 5 eV cloud
dimension, the energy transfer efficiency between the
plasma and the largely neutral shielding cloud was rather
low. Adding a small amount of energy from a ruby laser
pulse appeared to increase and sustain the energy transfer
efficiency according to the enhanced luminosity and

carbon line ionization intensities that were observed.
The small amount of laser energy probably led to increased
ionization of the cloud and hence to decreased mean free
paths and higher energy transfer from the hot plasma.
This enhanced plasma-cloud energy transfer persisted long
after the termination of the laser pulse.

CHAPTER II

THEORETICAL AND EXPERIMENTAL REVIEW

This chapter presents some of the results of the most recent theoretical models for plasma and laser interactions with solids and the assumptions used to derive their conclusions. Experimental work performed over the last few years in the areas of plasma-solid interactions, laser-solid interactions, and methods of X-ray generation are also reviewed. The discussion draws together the various aspects of the interaction processes that may take place in this particular experiment, although it is not intended to be an exhaustive review.

Plasma-Solid Interaction

When a pellet is exposed to a hot, dense plasma, its surface rapidly heats up and molecules are vaporized by electron bombardment. As soon as the ablation cloud forms, it begins shielding the pellet from the incident plasma electron energy flux, F_e, due to elastic and inelastic collisions. This shielding layer of expanding pellet material may make it possible for the fuel to penetrate sufficiently deep into a reactor plasma.

5

Recently a general model for the transonic flow of ablating pellet material applicable to a wide class of plasma conditions has been developed by Parks.[11] In order to minimize the pellet mass for optimum injection energy economy for a given penetration distance, this theory tends to favor injection in large reactors with high electron density, n_e, and low electron temperature, T_e. Initial assumptions inherent to this theory are a quasi-steady ablation rate (the pellet surface regression speed, $\dot{r}_p$, is slow with respect to the time of cloud formation) and the development of a physical shock front far from the pellet surface such that it has no effect on the absorbing portion of the primarily neutral cloud. The incident plasma energy flux either passes through the cloud unaffected or contributes to an increase in the enthalpy and kinetic energy of the ablating particles. The most important mechanism in the interaction is the energy absorption by the neutrals, which display gas dynamic motion. This mechanism almost completely controls the ablation rate and directly couples back to surface vaporization. With these considerations in mind, an analytical transport model evolved that describes the electron energy flux at any point in the cloud all the way down to the pellet surface. It is shown that the pellet surface regression speed scales as

$$\dot{r}_p \sim n_e^{1/3} r_p^{-2/3} T_e^{\frac{1}{2}} \gamma^{-2/3} \qquad (II - 1)$$

where r_p is the instantaneous pellet radius and γ is an "effective energy flux cross section."[11] Included in γ is an energy dependent loss function, $L(E)$, which accounts for the physical properties of the gas medium. The loss function explains the partitioning of an incident electron's energy among various processes, and, for evaluation, requires a knowledge of individual ionization cross sections such as primary ionization, dissociative ionization, double ionization, production of secondaries, discrete-state excitations, and numerous higher-order ionizations and recombinations.[12] It is thus an indirect function of T_e, varying for different gases. A semi-empirical fit for energies as low as 20 eV has been made of $L(E)$ for molecular hydrogen.[13] Thus, it is possible to predict a scaling law for the life time of a hydrogen pellet:[14]

$$\tau_p \sim \frac{r_{po}}{\dot{r}_p} \doteq \left. \frac{r_{po}^{5/3}}{n_e^{1/3} T_e^{1.71}} \right|_{H_2} \qquad (II - 2)$$

where r_{po} is the initial pellet radius. Notice the strong dependence on T_e as opposed to the weaker dependence on n_e, as well as the nonlinear relationship with the initial pellet radius. Considering the flow of energy carried by incident plasma particles across a

surface, Vaslow[15] obtained a similar dependence on the
pellet radius and density. The revised work of Milora
and Foster[16] is also in agreement. Gralnick[17] previously
derived a surface regression speed, using volume heating
by plasma ions, that showed no dependence on the pellet
radius. He assumed a linear relationship between the
ablation rate and the local plasma density, as opposed to
the relationships of Eq. (II - 1).

The respective individual cross sections of a poly-
styrene gas that contribute to L(E) are not well known.
The perhaps questionable assumption is therefore made
that the polystyrene cloud has the same form for L(E) as
does molecular hydrogen, and that Eq. (II - 2) is the
applicable scaling law for this case. Therefore, by
substituting $\Delta r_p / \Delta t$ for $\dot{r}_p$ in Eq. (II - 2), it follows
that

$$n_e^{1/3} T_e^{1.71} \doteq K(r_{po})^{2/3} \Delta r_p, \qquad (II - 3)$$

where Δr_p corresponds to the measured change or reduction
in the pellet radius, and K is a proportionality constant
containing, among other things, the pellet-plasma inter-
action time, Δt. The actual power of T_e depends on the
loss function for a particular gas.[11] Using the proper
L(E) would make a small correction which appears to fall
within the experimental error of this work since the

experimental results agree with the theory for pure H_2.
One qualitative explanation for this effect would be that
the smaller, lighter hydrogen molecules and ions readily
escape after dissociating from the polystyrene molecule.
The remaining carbon atoms and carbon-hydrogen molecules
cannot disperse (or be ionized) as readily during the
short interaction time of this experiment. A spatially
resolved spectroscopic analysis during the interaction
and a chemical analysis of the pellet surface carbon con-
centration after the interaction would help verify this
argument.

According to Eq. (II - 3) one needs to know the
average values of the electron density and temperature
during the interaction time, in addition to the initial
and final values of the pellet radius, to verify the
scaling laws. Specifically, a plot of the plasma param-
eters on the left-hand-side of Eq. (II - 3) against the
pellet parameters on the right-hand-side should result in
a linear curve, if the nonlinear dependences of the
scaling laws are indeed true.

The effectiveness of the shielding pellet cloud
varies mainly due to the dependence of τ_p on the five-
thirds power of the initial radius. Milora and Foster[16]
explain this nonlinear behavior by noting that as pellets
become smaller, they behave more like point sources of

mass for which the shielding clouds dissipate more
rapidly in space and become less effective. They deter-
mined that 5 μm would be the approximate hydrogen pellet
size below which the neutral gas shield is rendered
ineffectual (smaller pellets would require extremely high
velocities to reach the interior of hot plasmas). Inter-
preting the total luminosity of the cloud as being propor-
tional to the rate at which the pellet surface supplies
neutrals to the plasma, indirect measurements of the
ablation rates, showing agreement with the scaling laws,
recently have been performed.[16] In that study 210 μm
diameter frozen hydrogen pellets were injected into the
edge plasma of ORMAK at speeds of approximately 100 m/sec.

Laser-Solid Interaction

The interaction between a laser beam and its target
needs to be well documented and understood because of its
importance to laser weaponry, X-ray generation, laser
fusion, laser machinery, etc. In general, the presence
of a background gas, the reflectivity of the target sur-
face, the surface quality and finish, the laser wave-
length, and the pulse duration are all important param-
eters that modify the process and must be specified for a
given experiment. The development of the interaction
process occurs as follows:

a. Absorption in a skin depth for metals (or by impurities or imperfections for non-metals),

b. Heating and vaporization of the surface,

c. Breakdown in the vapor,

d. Expansion of the plasma and formation of a density gradient,

e. Generation of plasma shock waves (absorption waves),

f. Momentum transfer to target from moving plasma,

g. Generation of shock (stress) waves in the target,

h. Burn off of "late" plasma vapor by the hot plasma,

i. Dissipation of the plasma through radiation, etc.

The laser energy absorption process depends on whether the irradiated solid is transparent, reflective, or absorptive. If it is transparent, absorption occurs at the lattice irregularities or impurities at or inside the surface, and the situation is quite similar to gas breakdown. Whatever the source of the first electrons (multi-photon absorption, stimulated Raman scattering, impurities, stray ultra-violet radiation, etc.), a few do occur above the threshold and start the avalanche effect that leads to the generation of a strongly absorbing layer on the target surface. The development is then independent of the conductivity of the target.[18]

For metallic targets the initiation is more straight-forward. Here the initial conductivity of a smooth surface is quite high. Radiation falling on this surface interacts with the conduction band electrons in the skin depth. These electrons then respond collectively to the field, and energy is absorbed through free-free inter-actions, or collisions of electrons with imperfections, etc.[18] The general conclusion is that if adequate power density falls on the surface in a sufficiently brief time, vaporization will occur.[19]

As soon as the surface reaches the material vaporiza-tion temperature, the rate of evaporation is determined by energy conservation considerations. The regression speed (erosion rate) of the vapor-solid interface of a flat surface may be expressed as[18]

$$U_s = \frac{I_o}{\rho_s(C_s T_m + L_m + C_\ell(T_v - T_m) + L_v)}, \quad (II - 4)$$

where I_o is the laser power density, ρ_s is the solid den-sity, C_s and C_ℓ are the specific heats of the solid and liquid, respectively, T_m and T_v are the melting and vaporization temperatures, and L_m and L_v are the latent heats of melting and vaporization.

After a "short" time (less than the laser risetime) the density profile near the target surface can be sketched as shown in Fig. II-1. The absorption of laser
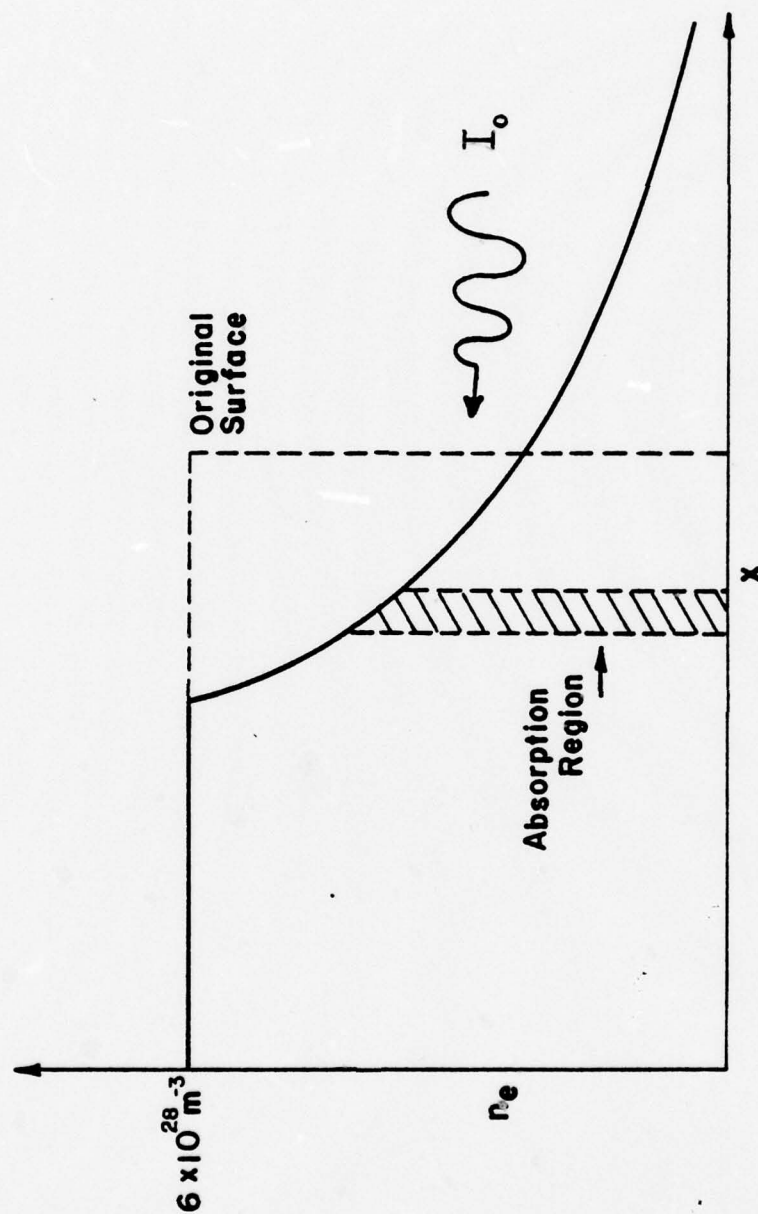
Fig. II-1. Target Density Profile During Irradiation.

radiation in the target gas, assuming inverse brems-
strahlung, follows a Bougeur's Law relation:

$$I = I_o \exp(-x/\ell_{ab}) \qquad (II - 5)$$

where the "absorption length" is given by[20,21]

$$\ell_{ab} = \frac{1.28 \times 10^{18} \nu_o^2 T_e^{3/2} (1 - (\nu_p/\nu_o)^2)^{1/2}}{Z n_e^2 \ell n(\Lambda(\nu_o))}, \qquad (II - 6)$$

where ν_o is the laser frequency, ν_p is the plasma frequency
given by

$$\nu_p = \frac{1}{2\pi}\left[\frac{n_e e^2}{\varepsilon_o m_e}\right]^{1/2}, \qquad (II - 7)$$

and

$$\Lambda(\nu_o) = \frac{(T_e)^{3/2}}{2\pi \nu_o Z e^2 m_e^{\frac{1}{2}}}. \qquad (II - 8)$$

In Eqs. (II - 6 & 8), T_e has the units of electron volts.
The absorption length decreases with decreasing tempera-
ture and increasing densities near the surface until a
"critical frequency" is reached when $\nu_p \doteq \nu_o$, beyond
which there is no propagation and the laser radiation may
be totally cut off from the surface. Further interaction
with the target is by plasma heat conduction and pres-
sure. Damage to the ablating target depends on time.
Apart from burning through the target material, the
impact of the laser radiation can cause "impulse loading,"

which in principle causes fracture, plastic deformation, spallation, etc.

When the ionization cross section in the vapor is sufficiently large to absorb the laser energy, the process can then grow to breakdown. An "overdense" opaque plasma has been observed to decouple the laser from the target,[22] and the absorption region (at critical density) propagates up the beam in the form of a "detonation wave," or a "combustion wave," depending on the laser flux level.[18] This wave is driven as long as there is laser energy being deposited behind the density front. For high flux densities the front steepens and travels as a supersonic laser-supported detonation (LSD) shock wave, while for low flux densities the absorption region is thin and the front propagates subsonically as a laser-supported combustion (LSC) wave. The gas behind the LSC wave is in the form of a plasma in pressure balance with the surroundings. An analysis of laser absorption waves (LAW) was developed in the Soviet Union by Raizer.[23]

In the case of breakdown in the atmosphere, the threshold for gas breakdown is well above the threshold for propagation of the LAW's. However, the generation of these waves in the interaction of laser radiation with solid surfaces occurs at rather unexpectedly low irradiance values, and the ignition mechanism (the mechanism

responsible for the initial LAW generation) has been the subject of much speculation. Threshold values between 2×10^9 and 6×10^{10} W/m^2 (below the threshold for plasma generation from laser-solid interactions in a vacuum) were measured by Hall using a CO_2 laser with a 3 μs pulse and various target materials.[24] Recent experimental surveys suggest that thermionic emission and local target heating play major roles in the ignition mechanism for LAW's on practical aluminum surfaces.[25,26] The roles played by chemical reaction, shock-heating of the gas, and nonequilibrium ionization of the vapor in the transfer of energy from a laser beam to a surface in the presence of a gas atmosphere are still largely unknown. This low-threshold generation of LAW's is a limiting effect on the amount of laser energy that can be deposited on the surface.

X-ray Generation

The generation of X-rays from dense high-energy plasmas produced by high-power pulsed sources has stimulated considerable interest because of the large number of possible applications, which include diagnostic techniques, simulation of weapons effects, and even the development of a soft X-ray laser.[27] The transformation of plasma energy into radiation due to the presence of

high Z impurity atoms is recorded in the literature for a
variety of experiments.[28,29,30] For instance, the dense
plasma focus produces X-radiation resulting largely from
the impurity ions which come from the electrodes and
interact with hot, dense plasma.[31] Impurities can be
selectively introduced (from thin foils, etc.) in a pre-
formed clean plasma.[32] This procedure reduces the radia-
tion losses that would have been experienced during the
plasma formation and heating phases if the impurities were
initially present. A theta pinch device is also well
suited for this application since the cylindrical plasma
can form and then radially implode on a pellet at its axis.

The efficiency of transferring plasma energy to X-
radiation will vary between experiments, but one of the
highest is that of the dense plasma focus. It has
approximate efficiencies of 0.03% and from 0.4 to 2.2% in
converting stored electrical energy into radiant energy
and plasma energy, respectively.[33,34] The plasma energy
may be further utilized to produce radiation through
interactions with solids. However, the energy ultimately
going into X-rays would be much less than 1.0% when the
dense plasma focus is used as the radiation source.

Another popular method of X-ray production is the
bombardment of solid targets with energetic heavy ions.
In recent work, 5 to 7 keV X-rays were produced by

bombarding thin aluminum foils with low Z ions such as MeV proton and helium-3 ions[35] and 0.4 to 20 MeV neon ions.[36] It appeared that the X-rays were bremsstrahlung from secondary electrons ejected from the target. Again, however, the more energetic X-rays represent less than one percent of the incident energy.

Other experiments produced X-rays from hot, dense plasmas formed by irradiating small pellets with high power laser beams.[37,38] The temperature and density of a laser-produced plasma on a plane thick target are rapidly varying functions of the distance from the target. A plasma produced at the surface of a $(CH_2)_n$ target irradiated by a 1.06 µm Nd laser with flux densities up to 10^{16} W/m^2 had electron temperatures and mean densities of around 200 eV and 4×10^{26} m^{-3}, respectively, within 100 µm from the target surface.[39] The lifetimes of the hot ions were less than a nanosecond, and the plasma density dropped by more than an order of magnitude within a few tens of microns from the surface. The same experiment showed the following dependence of the peak electron temperature on the laser power density, I (W/m^2):

$$T_e \doteq 1.34 \times 10^{-3} I^{2/3} \quad \text{(eV).} \quad \text{(II - 9)}$$

This result agrees with those from a time independent model for the energy absorption mechanism.[40] Other

conclusions were that the electron energy distribution was Maxwellian, the inertial confinement time of the ions was proportional to the temperature, and that most of the laser energy was absorbed at very high densities (10^{26} to 10^{27} m^{-3}) within a few tens of microns from the target surface.[39]

McMordie and Simmons[41] reported X-ray emission studies of CO_2 laser-produced plasmas for target elements covering the atomic number range $6 < Z < 92$. The X-ray fractional yield was less than 3×10^{-6} for irradiations around 7×10^{14} W/m^2. Their experimental results exhibited a dependence of the plasma electron temperature (100 to 150 eV) on the laser peak power flux of the form $T_e \sim I^n$ where n is approximately 0.32 (0.25) for carbon (titanium). Titanium and iron targets apparently showed the greatest yield. The X-ray energy emission from plasma bremsstrahlung radiation transmitted through a foil is:[6]

$$E_{ff} = 1.42 \times 10^{-34} Z n_e^2 T_e^{\frac{1}{2}} V \tau_p \alpha \quad (J), \quad (II - 10)$$

where Z is the atomic number, n_e the electron density, V the plasma volume, τ_p the plasma duration, and α the fraction of total energy transmitted through the foil window. Applying this result to the previous experiment yields a peak energy which is $\doteq 30\%$ smaller than the experimental result. Recombination radiation probably

accounts for the difference.

A plasma produced when a giant pulsed ruby laser of 5 J energy and 17 ns duration was focused into a 300 μm diameter spot on a polyethylene target in vacuum had peak electron temperatures and densities of about 100 eV and 10^{24} m^{-3}, respectively, both of which fell off an order of magnitude at 10^{-3} m from the target surface.[42] It was estimated that the electron temperature, the ionization energy, and the energy lost by radiation and target recoil accounted for only 10% of the incident laser energy. This fact implied that 70 to 80% of the laser energy at power densities of 2.9×10^{15} W/m^2 was converted into ion kinetic energy. Also, it was shown that only 4% of the carbon atoms in the exposed polyethylene were ionized; the rest of the target material presumably absorbs the recoil from the plasma jet.[42]

Assuming classical absorption for the case of a diamond or aluminum target irradiated by 10^{12} W from a mode-locked laser, the electrons in the target conduction band can gain energies on the order of 1 keV in less than a picosecond.[43] This energy would be sufficient to further ionize the core electrons. Calculations by a Livermore group[44] showed that the implosion of solid pellets by an array of lasers could increase their density by a factor of $\doteq 10^3$. These conditions would

make it possible to obtain an X-ray laser at 0.1 nm wavelength under suitable conditions.[27]

Using Battelle's HADRON/CILAS VD-640 neodymium-doped-glass laser with solid iron and copper slab targets, Mallozzi et al[45] conducted a study to understand better the X-ray output spectrum with efforts directed towards increasing the overall yield and average photon energy. Focusing the twelve 110 J, 3.5 ns, 1.06 μm pulses onto the targets, they were able to convert Nd laser light into X-rays with an efficiency greater than 25 percent (referring to the portion of the X-ray spectrum above approximately 300 eV emitted uniformly into 2π steradians away from the slab). Another principal result of their time-dependence measurements was that the radiation fairly closely follows the laser input intensity, verifying the quasi-steady picture of the X-ray production model. This finding implies that the X-ray pulse can be formed into a desired shape by tailoring the laser pulse. In an earlier investigation it was determined that the bulk of X-rays were produced by spectral lines emanating from the relatively cool (< 1 keV) leading edge of a thermal diffusion front.[46] A hard radiation component was emitted from a hot low density region with ≐ 1% conversion efficiency, and corresponded to free-free plus free-bound radiation at ≐ 5 keV electron temperature.

Due to a high conversion efficiency more than 10^4 J/m^2 of soft X-rays were delivered to a usable area, free of debris.

A plasma model with one dimensional, quasi-steady, compressible, inviscid fluid flow yielded some ready formulas for the plasma temperature, plasma thickness, and average ion density:[46]

$$T_{e\infty} \doteq (I_o/\sigma)^{1/4}, \qquad (II - 11)$$

$$d \doteq v_\infty \tau_o = ((\overline{Z^*_\infty} + 1)k/M)^{\frac{1}{2}}(I_o/\sigma)^{1/8}\tau_o, \qquad (II - 12)$$

$$(n_1)_{av} \doteq \frac{M^{\frac{1}{2}}\sigma^{3/8} I_o^{5/8}}{6(\overline{Z^*_\infty} + 1)^{3/2}k^{3/2}}. \qquad (II - 13)$$

In the above equations I_o is the laser intensity with pulse-width τ_o, σ is the Stefan-Boltzmann constant, v is the fluid velocity, $\overline{Z^*}$ is the mean effective ion charge, k is the Boltzmann constant, and M is the ion mass. The subscript ∞ indicates quantities out to a given distance, after which the quasi-steady conditions break down. These conditions are no longer valid when the characteristic time for hydrodynamic expansion or contraction, τ_h, satisfies the relation[46]

$$\tau_h \le \frac{10^{12}}{n_e}. \qquad (II - 14)$$

Therefore, at distances far enough from the surface where n_e is sufficiently low Eq. (II - 14) will be satisfied.

A fourth method of generating radiation is to use intense laser beams in combination with hot plasmas to irradiate small pellets and other targets. An investigation of this approach is reported in this dissertation. Again the linear theta pinch configuration facilitates such experiments by permitting axial entrance for the incident beam as well as ease of access to the generated radiation. There are several possibilities for the sequence of pellet-plasma-laser interactions. A larger portion of the plasma energy could be converted to radiation, rather than used for pellet vaporization, by first hitting the pellet with the laser beam and producing a small volume of plasma or neutral atoms available for heating by the hot plasma. Another case would be to perform the laser irradiation after the initial pellet-plasma interaction such that the absorbed laser energy would produce some heating of the dense, low temperature plasma cloud around the pellet.

In summary, it appears that efficient production of energetic X-rays for short durations requires pulsed laser energies. For longer durations, less efficient X-ray production may be achieved with hot, dense plasmas that are well contained. An initial goal of this work

was to determine if a combination of these effects would result in the efficient production of energetic X-rays for relatively long durations.

CHAPTER III
EXPERIMENTAL ARRANGEMENT AND METHODS

In order to expose a pellet to a hot, dense plasma
under reproducible conditions, a well-understood plasma
source and a means of accurately locating the pellet with
respect to the plasma were needed. This chapter dis-
cusses the general experimental setup used to study
pellet-plasma-laser interactions. The plasma source is
described briefly, while considerable emphasis is placed
on the pellet measurement and positioning techniques and
some care is taken to point out the most likely causes of
experimental error. Assumptions and data treatment
necessary to relate the findings to current theory are
presented in detail, and the diagnostic methods are also
discussed.

Theta Pinch System

The general TeePee 1B theta pinch experiment that
was used as a plasma source is shown in Fig. III-1, which
includes some of the typical circuit parameters.
Nunnally[2] describes explicitly the design considerations

25

Fig. III-1. Theta Pinch Circuit Diagram and Typical Parameters.
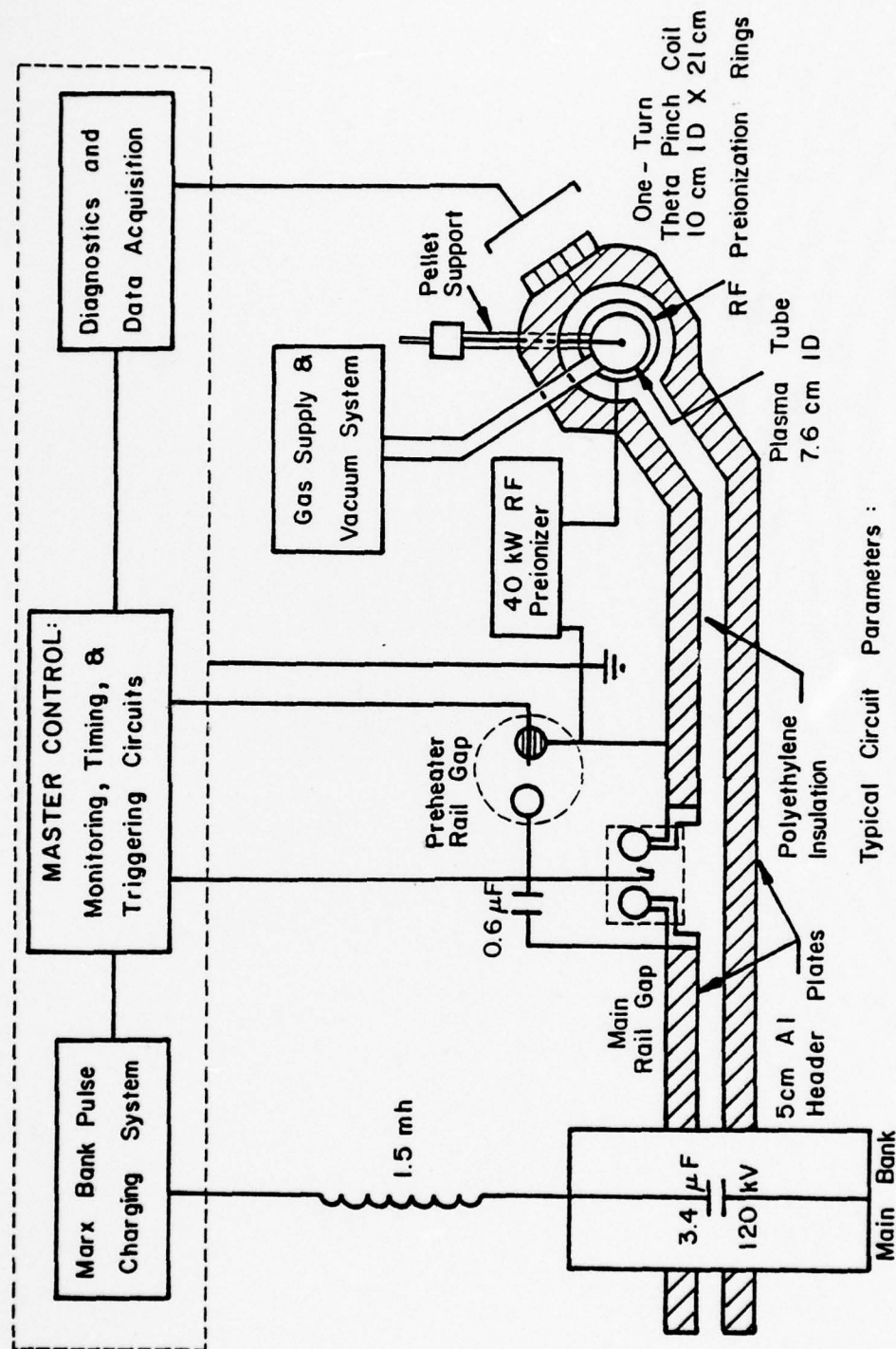
Typical Circuit Parameters:

Charging Voltage ~ 70 kV   Quarter Period ~ 1.2 μs
Theta Coil Inductance ~ 40 nH   Maximum Current ~ 400 kA
Total Circuit Inductance ~ 220 nH Maximum Magnetic Field ~ 2.3 T

and operation parameters of the TeePee 1A of which the TeePee 1B is a slight modification. Hence, only a short review of this machine will be given. Originally established as a very fast experiment for studying particle end-losses, this theta pinch has been used for previous pellet-plasma-laser studies[2] and as the object of Thomson scattering investigations.[47]

The 3.4 μF main capacitor bank of the TeePee 1B was capable of a maximum stored energy of 24 kJ. It was discharged through a field-distortion triggered rail gap and around a single-turn coil with a 0.21 m length and a 0.10 m bore. The energy was coupled, through transformer action, into the preionized, preheated, hydrogen plasma inside the coil. A 40 kW, 14 MHz RF oscillator of variable pulse length (≐ 500 μs) was used to break down and preionize the research grade hydrogen gas at initial static filling pressures from 15 to 90 mTorr as measured by an MKS Baratron Pressure Head, type 77. The main capacitor bank was pulse charged with a six stage, ignitron triggered, Marx generator so as to be fully charged at the termination of the RF oscillations. The low inductance 0.6 μF preheater capacitors which shunted the main rail gap were switched into the main circuit by another triggered rail gap,[2] about five microseconds before the main gap was fired. The resulting resonant

circuit caused a small portion of the main bank energy to ring out across the theta coil at a frequency of approximately 1.4 MHz, producing a maximum magnetic field of 0.15 Tesla. The initial shock heating of this rapidly damped oscillation further preionized the gas ($\doteq$ 40%) before the main theta discharge.

Plasma heating was achieved by some adiabatic compression and ohmic heating due to induced currents in the plasma when the main rail gap was fired, but largely by the shock wave heating as the $\overline{J}$ x $\overline{B}$ forces swept the ionized gas rapidly inward to form a cigar-shaped plasma of about 0.01 m diameter. Typically, for this work, the main bank was pulse charged to 70 kV with a corresponding maximum discharge current of about 400 kA. The quarter period during which the magnetic compression field flux density reached its maximum amplitude of 2.3 T was less than 1.2 μs. The five centimeter thick aluminum header plates had a total circuit resistance of 23 mΩ. About one-fifth of the total circuit inductance of 220 nH was in the single-turn coil.

Based on earlier measurements, the time and space resolved plasma parameters were well documented for the first quarter period of the discharge. The electron temperature has been analyzed by diamagnetic probes, soft X-ray foil detectors, and Thomson scattering, while the

electron density was measured according to image converter camera data, Mach Zehnder interferometry, and Thomson scattering.[2,47] One of the more obvious characteristics of this plasma was its radial hydromagnetic oscillations or rapid inertial "bouncing" ahead of the main magnetic compression field. This effect is demonstrated by the time variations of T_e and n_e at the center of the cylindrical plasma in figures III-2 and III-3, respectively.

Circuit Modifications

The major difference between TeePee 1B and TeePee 1A was the replacement of the original low-inductance dielectric switch package and electrode assembly[2] by the main rail gap and a high voltage, fast risetime triggering arrangement. The primary reason for this change was to speed up the experimental operation and data acquisition. The pressurized rail gap, made by Maxwell Laboratories, Inc., was carefully installed such that the overall circuit inductance was increased by only 20%. The compression electrode contact of the preheater circuit was replaced with eight parallel, 0.30 m lengths of RG-8/U co-axial cable that went around the rail gap under the surface of the oil bath covering the header plates. Thus, the inductance and ringing frequency of the preheater circuit changed very little.
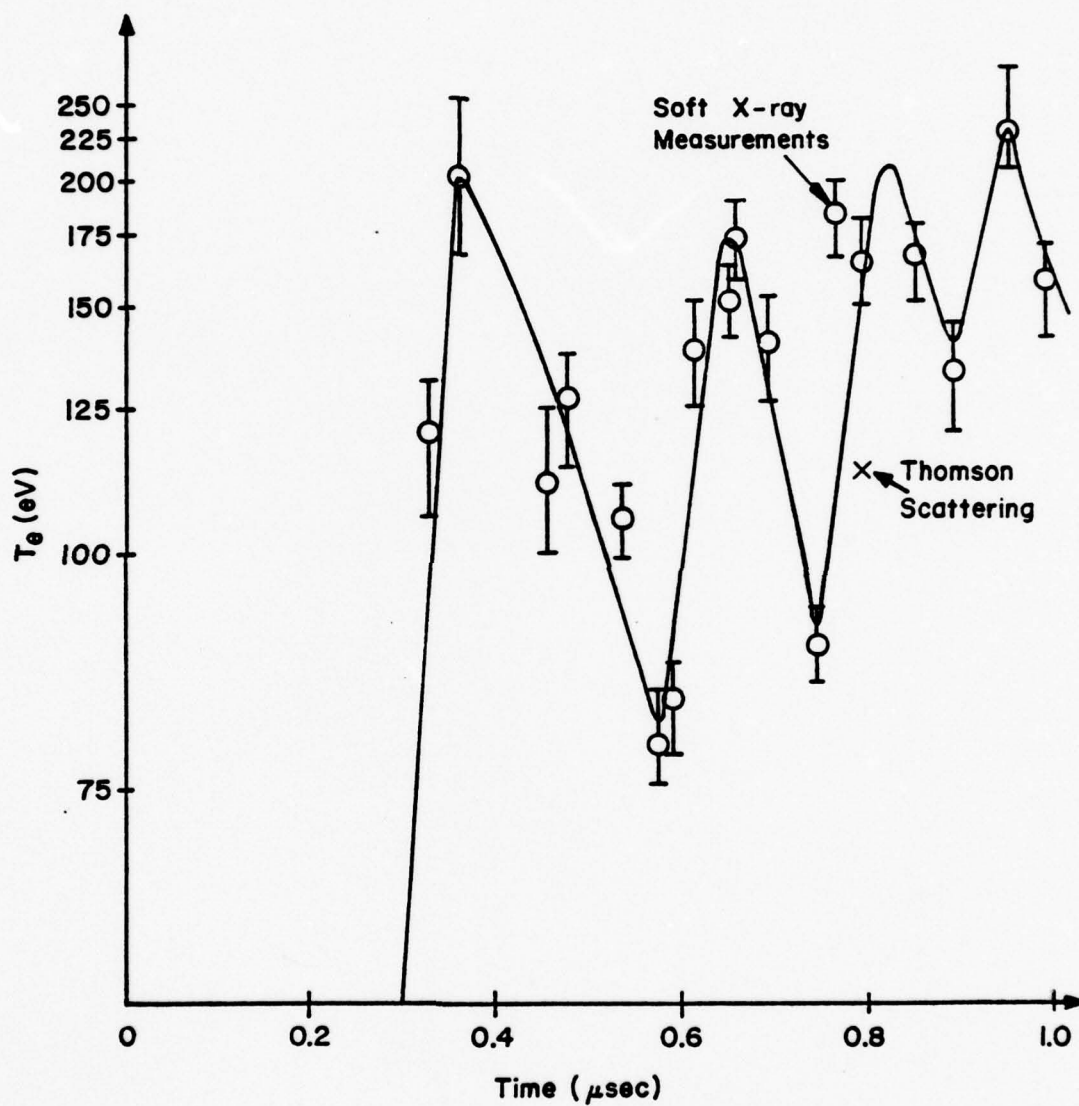
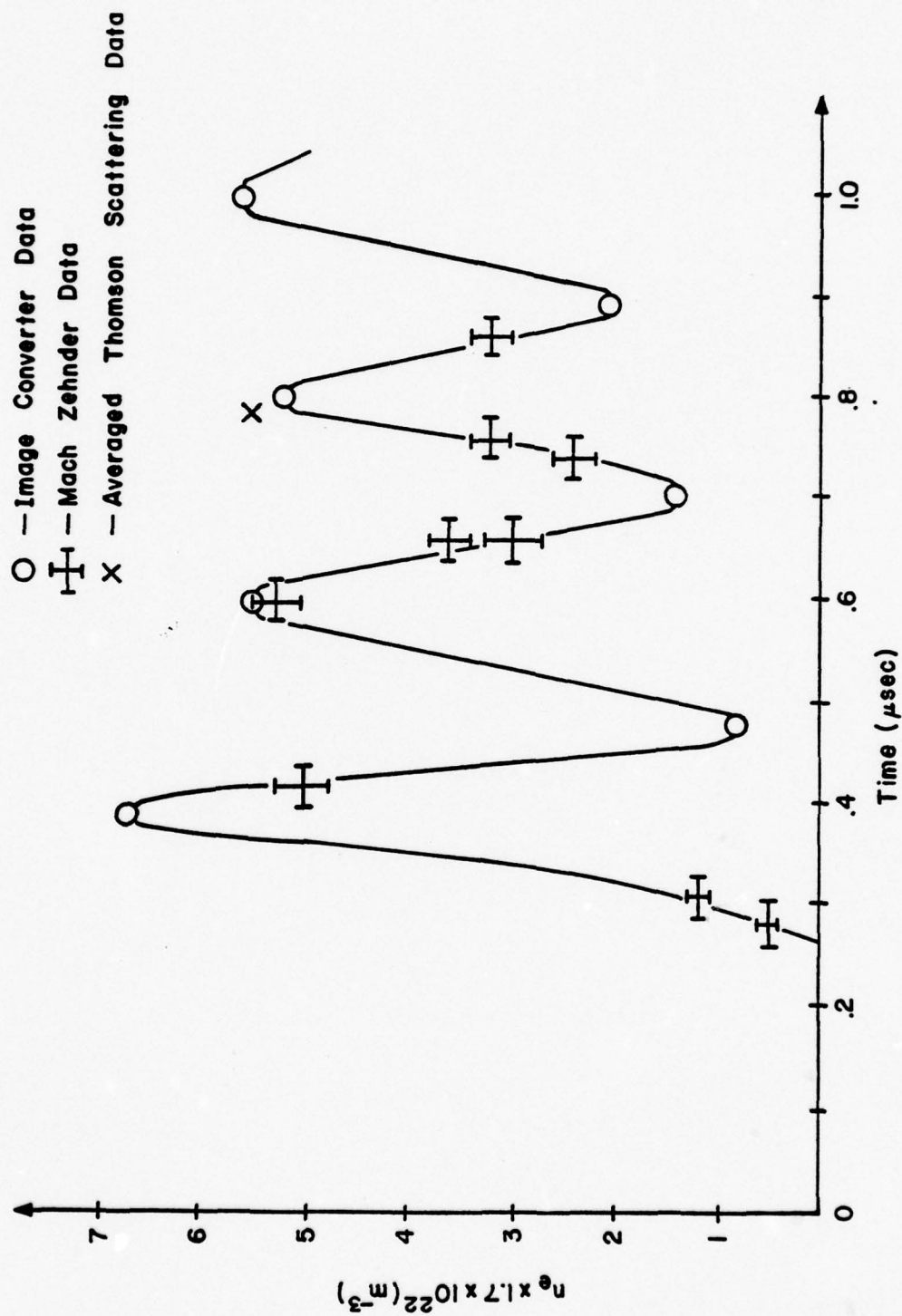Fig. III-2.   Time Resolved Electron Temperature at 60
mTorr. (Ref. 2, 47).

Fig. III-3.   Time Resolved Electron Density at 60 mTorr.   (Ref. 2, 47).

In spite of attempts to operate at reduced pressures
of various gases (nitrogen, dry air, sulfur hexafluoride,
etc.) and to keep the gap housing as clean as possible,
difficulties persisted with high voltage tracking and
piercing through the thick lucite walls resulting in
destructive separation of the housing. The final solu-
tion was to operate in open air with appropriately
increased gap spacings. Specifically, the 0.10 m long
brass electrodes were separated by 0.047 m with a 0.018 m
spacing between the grounded electrode and a molybdenum
knife-edge (sheet) trigger electrode. The performance of
the gap turned out to be very repeatable, switching 70 kV
at 400 kA with the delay and jitter both less than 100 ns
and with no appreciable wear on the brass electrodes
except for a uniform discoloration and change in surface
texture (from a fine polish to a "sandblasted" type of
finish. Surprisingly little maintenance was necessary.
The only problem was the acoustical noise in the area
during operation.

A HEDS (High Energy Density System) pulser unit,
which had been part of an exploding wire experiment
designed by Field Emission Corporation for the Air Force
Weapons Lab at Kirtland AFB in 1966,[48] was used to trigger
the main rail gap. The pulser was built as a Marx-surge
device consisting of 26 stacked modules, each of which is

a potted LC pulse forming network as shown in Fig. III-4.
They are tightly fitted into an insulated metal casing
that serves as a pressure vessel, electromagnetic shield,
and common ground for the pulser circuit. Normally the
pulser was charged to 15 kV and pressurized with dry
nitrogen or air at about 20 psig. A 7 kV pulse applied
to the trigger pin between the spherical brass electrodes
of the first gap was sufficient to erect the entire unit
since all the other critically spaced gaps were rapidly
overvoltaged. A general description, operation require-
ments, and proper maintenance procedures of the HEDS
pulsers will be outlined in a laboratory technical
memorandum.[49]

The output from the pulser was conducted via an
RG-19 cable, about one meter in length, to the primary
(outer braid) of a 1:2 step-up high voltage co-axial
transformer as illustrated in Fig. III-5. The output
side of the primary was electrically connected to the
shielding braid of the RG-19 to form a return path
directly to the pulser ground, minimizing the inductive
load. Two loops of the inner insulation and conductor of
RG-8/U coaxial cable wrapped with polyethylene film for
extra insulation were fed through the primary braid to
form the transformer secondary. This step-up transformer
served the purposes of (1) providing the high voltage

Brass Spark
Gap Electrodes

Buttons for
compression contact
with next module

Side View

HV
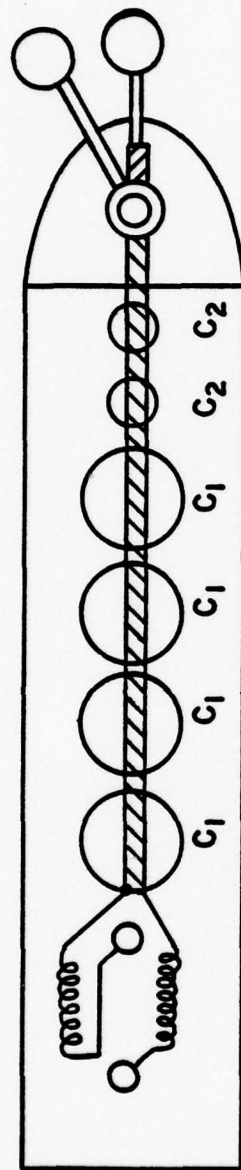
Top View

$C_1 \sim 1600\,pF$
$C_2 \sim 500\,pF$
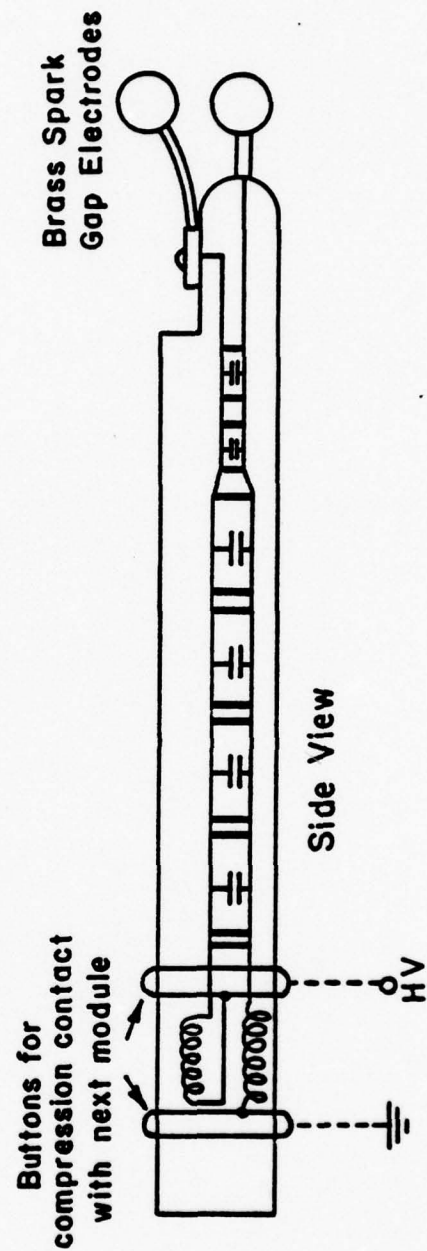
C_1 C_1 C_1 C_1 C_2 C_2

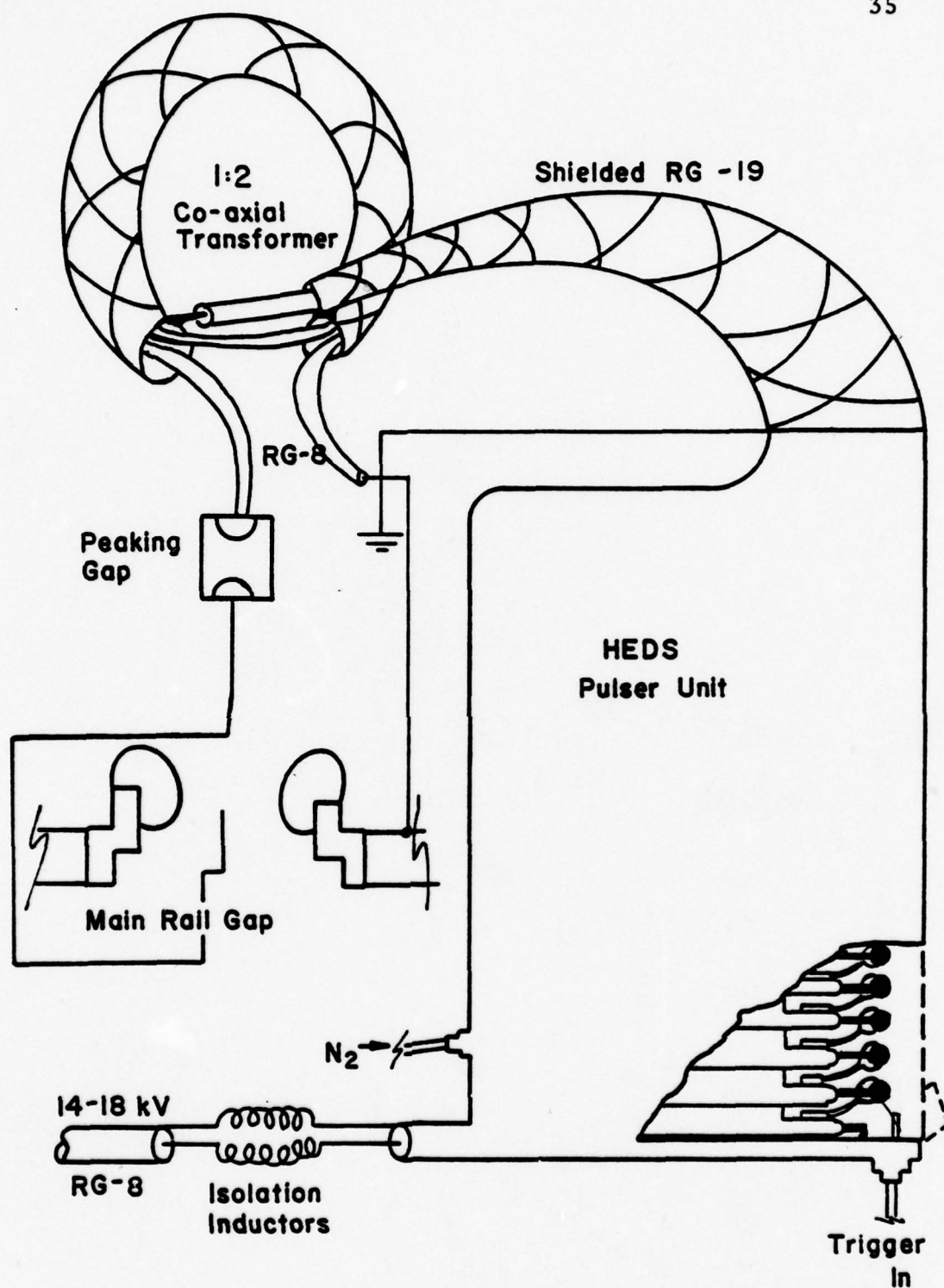Fig. III-4. One of the 26 Modules in the HEDS Pulser.

Fig. III-5.   Main Rail Gap Triggering Arrangement.

trigger pulse required for reliable switching of the main rail gap, (2) preventing damage to the HEDS pulser modules by isolating them from a reverse high energy common mode noise pulse of 70 kV that occurred when the rail gap fired, and (3) to break a possible ground loop. Actually, the transformer compensated for the large voltage drop across the RG-19 high voltage feed so that a large enough dV/dt ($\doteq$ 10 kV/ns) to result in uniform trigger discharges at the rail gap could be produced. Background theory on co-axial transformers and more details on this particular one is given in Appendix A. Finally, a peaking gap was used to get the best possible risetimes from this scheme.

A simple high voltage probe ($\leq$ 300 kV) with a good frequency response ($\leq$ 100 MHz) and high input impedance ($\geq$ 10 kΩ) was constructed of two concentric cylinders of conductive plastic of the type described in Appendix B and used to measure most of the voltages and risetimes of interest on the TeePee 1B experiment. It indicated that the output pulse at the co-axial transformer secondary was 300 kV with a rise time of approximately 30 ns. As a result the pulse between the molybdenum trigger electrode and the grounded brass electrode of the rail gap was indeed fairly uniform, according to visual observation. Typically one bright arc was formed in the air gap with two to six dimmer arcs located randomly along the entire

length of the electrodes. This fact and a uniform dis-
coloration of the brass electrodes indicated the current
density was well distributed and the gap inductance was
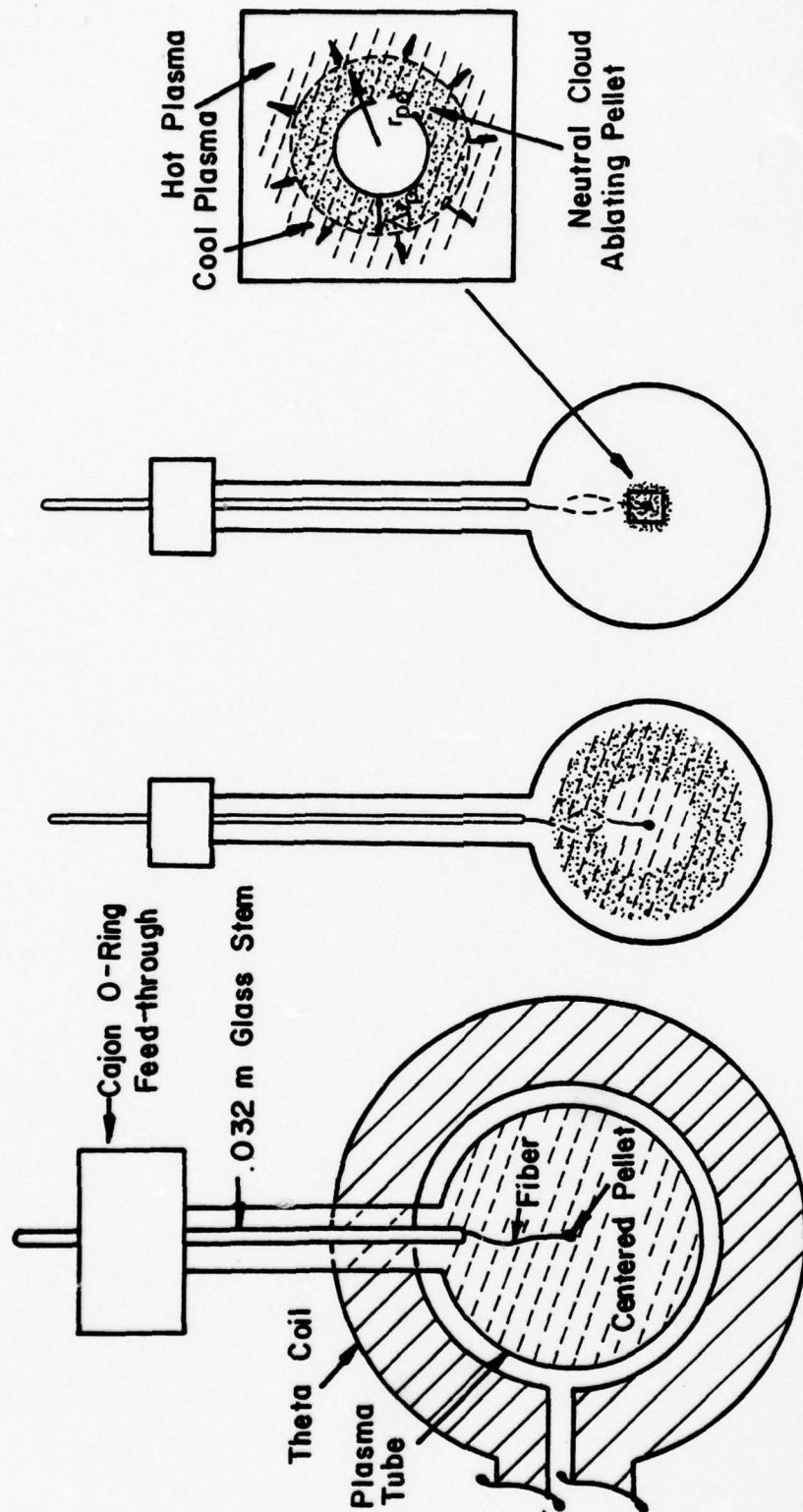minimized.

The HEDS pulser was designed for a low impedance
load; hence, the rapidly increasing voltage into an open
circuit created severe noise problems. Consequently,
considerable care had to be taken to isolate properly all
the electrical components in the theta pinch system and
insure that they all were connected to a common ground
with the least possible inductance in the leads. The
HEDS pulser triggering scheme of Fig. III-6 illustrates
some of the measures taken to isolate the various com-
ponents.

Pellet Suspension and Measurement

The phases of the pellet-plasma interaction in the
TeePee 1B as viewed along the axis of the plasma tube are
shown in Fig. III-7. The figure shows how the polystyrene
microspheres were attached to glass fibers having widths
of about 10% or less of the pellet diameters and which,
in turn, were fastened to glass rods by Permabond 101
glue (similar to Eastman 910). The pellet support
assembly was inserted through an O-ring seal so the
pellet could be manipulated and positioned at the focal

Fig. III-6. HEDS Pulser Triggering Circuit With Noise Isolation Measures.

38

Hot Plasma

Cool Plasma

Neutral Cloud
Ablating Pellet

Cajon O-Ring
Feed-through

.032 m Glass Stem

Theta Coil

Plasma Tube

Fiber

Centered Pellet

I Preionization Phase   II Preheating Phase   III Maximum Compression

Fig. III-7.   Interaction Sequence Between the Plasma and Suspended Pellet.

39

spot of a HeNe alignment laser without losing vacuum. (Clean-up shots could be made before lowering the target into position.) Hence, every pellet could be centered radially in the cylindrical vessel; however, there was some axial variation (± 0.005 m in the 0.21 m long coil) due to curling of the fibers. This affected the spectroscopic results, as explained later. Another likely source of error was the inability to control carefully the quantity of glue used with each pellet. This, unlike the essentially repeatable fiber mass, could amount to a non-negligible fraction ($\doteq$ 15±5% according to visual estimates of the glue volume) of the pellet mass. Photographs of typical pellets used in this experiment are shown in Fig. III-8. The transparent pellets act as spherical lenses and create special effects under certain illuminations. The pellet dropping mechanism used by Nunnally[2] was given serious consideration, but the random velocities at which the pellets fell into the plasma tube did not produce the repeatability required for the detailed measurements.

To determine the ablation rates, the diameters of the microspheres were measured along several major axes using a standard microscope and a translation stage, driven by a calibrated micrometer head, before loading them into the experiment and also after the theta pinch
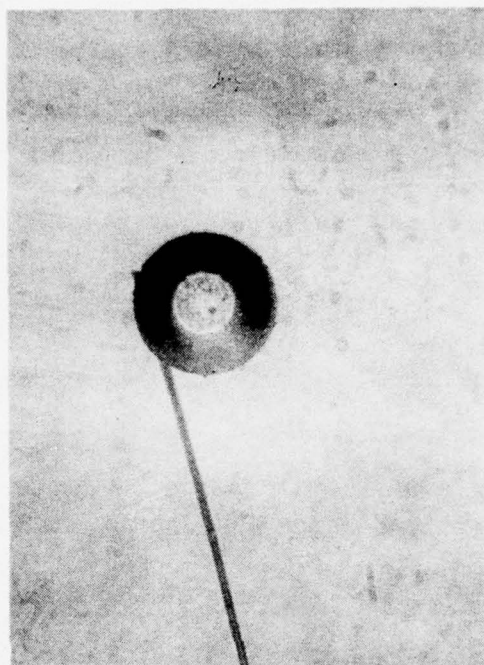
Fig. III-8.   Typical Polystyrene Pellets.

discharge (providing the samples could be located and recovered from the vacuum system). In order to measure the largest changes, the smallest, manageable pellets available were used. Since the pellets' radii varied from 50 to 150 microns, each one had to be measured separately. A typical error of one micron in the diameter measurements is largely responsible for the error bars in the resulting data.

Relating Data to the Scaling Laws

As mentioned earlier, the electron temperature, T_e, and density, n_e, of the plasma depend on the initial hydrogen filling pressure, P_o, and are nonlinear functions of time as the plasma undergoes radial hydromagnetic oscillations when it is shock heated by the rapidly increasing magnetic field. In order to consider ablation rates in the simplest case, it was necessary to assume the same fixed interaction time for different shots and different filling pressures, approximately 2 μs, during which the plasma remained clean and relatively hot. Also, since the average values of $n_e(t)$ and $T_e(t)$ need to be known over this interaction time, piecewise linear approximations of the nonlinear curves were made, and $\overline{n}_e$ and $\overline{T}_e$ were determined. The data would then represent a quasi-steady state plasma.

An example of this approximation is given in Fig. III-9 for $n_e(t)$ in the case of P_O = 60 mTorr. The solid curve is based on data[2,47] taken before the circuit modifications discussed in a previous section were made. The data points with estimated error bars represent Mach Zehnder interferometric measurements (like those described by Nunnally[2]) performed after the circuit modifications. It can be seen that the results are generally unchanged. (Time t = 0 in the figure corresponds to when the main rail gap fired and triggered the main bank discharge around the theta coil.) Since this information is also supported qualitatively by streak camera photography, it is assumed that T_e and n_e for other filling pressures are not appreciably different from the piecewise linear approximations of the earlier data. It should be noted that the last linear section of Fig. III-9 is purely an extrapolation, but the possible discrepancies would contribute an error that is small with respect to the error bars already associated with $\bar{n}_e$ and $\bar{T}_e$.

Spectrometer and Laser Systems

The relative carbon line ionization intensities were monitored with a Jarrel Ash 0.5 meter Ebert monochromator, Model 82-010. The carbon lines CI, CII, CIII, and CIV were observed during the pellet-plasma-laser interactions
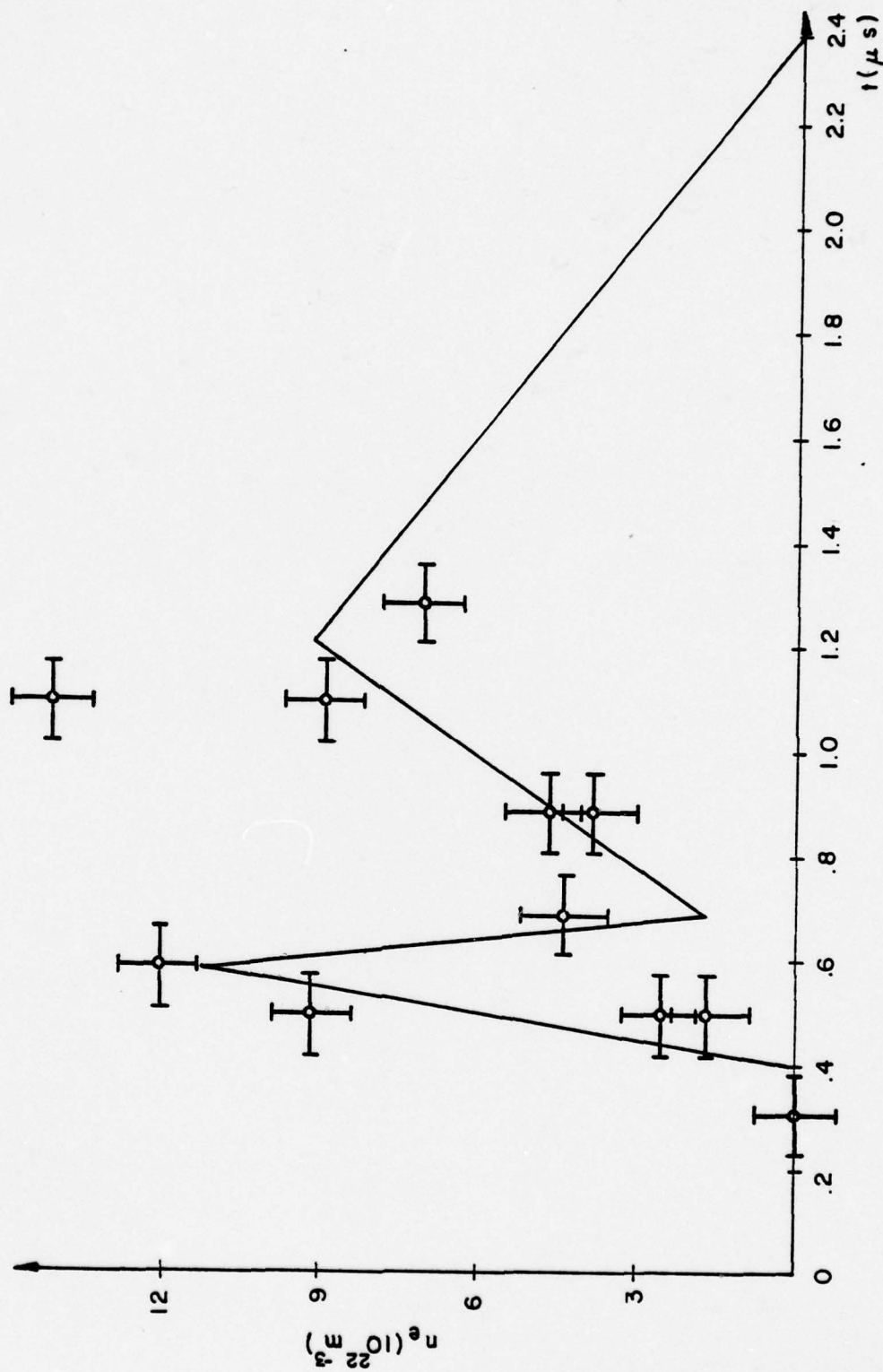
Fig. III-9. Linearized Approximation of $n_e(t)$ for P_O = 60 mTorr.

44

through a fiber optic light pipe that was butted up
against the plasma tube to face the pellet. By adjusting
the amplitudes of the various carbon lines according to
the appropriate spectral efficiencies of the fiber optics
and EMI 9558B photomultiplier tube, it was possible to
compare the intensities of the subsequent ionization
stages and estimate the temperature in the ablation cloud
by using the calculated values of Table I. The relative
population of the higher ionization levels of the pellet
cloud system is controlled by the dominant collision
processes. This system can thus be considered in coronal
equilibrium,[50] in which case the ratio of the line inten-
sities is independent of n_e, being a function only of
T_e.[51]

A Q-switched, Holobeam, series 301, ruby laser
system was focused through a quartz window on the center
of the theta coil mid-plane where the pellets were fixed.
It produced a 30 ns FWHM pulse of approximately 2.5 J, as
measured by a Quantronix Model 500 "Energy Receiver."
For a focal spot diameter of 0.002 m it was capable of
delivering ≤ 0.1 J to an average pellet. The Q-switch
Pockel's cell of the laser could be triggered with a TRW
Model 46A Trigger Delay Generator at any time during the
theta pinch discharge. The timing of the light pulse
with respect to the magnetic field was monitored with an

Table I

**Electron Energies Determined from Equal Intensities
of Subsequent Ionization Stages of Carbon (Ref. 2)**

Ionization Stage	T_e	λ
CI		600.6 nm
	1.05 eV	
CII		426.7 nm
	2.5 eV	
CIII		569.5 nm
	5.6 eV	
CIV		465.8 nm
	8.2 eV	
CV		
	82 eV	
CVI		
	110 eV	
CVII		

ITT FW114 planar diode terminated in 50 ohms. The laser-pellet-plasma interaction scheme is shown in Fig. III-10.

As an alternative to the visible 694.3 nm wavelength, it seemed desirable to use a CO_2 laser pulse at 10.6 μm and try to heat up the ionized pellet vapor even further. Attempts were made to use the 100 MW, 200 ns pulse length, CO_2 TEA laser described by Molen.[52] By the nature of its design, however, it was inherently sensitive to the electromagnetic noise generated by the theta pinch system and would always fire when the main rail gap was triggered, before the formation of the hot plasma. Hence, only qualitative pellet-CO_2 laser interactions were observed in a near vacuum.

A TRW Model 1D image converter camera was used primarily in the streak mode to monitor, photographically, the plasma formation and the pellet-plasma-laser interactions. Viewing in the radial direction through a slit in the theta coil with the magnification of a f/0.5, 0.20 m diameter relay lens, it was possible to record the theta pinch plasma and pellet cloud diameters versus time and the occurrence of the laser pulse. Like the spectrometer photomultiplier, the sensitive electronics in the camera required that it be enclosed in a double walled screen room or Faraday cage. Similarly all signals taken from the experiment (e.g. magnetic field probes, etc.)

Beam
Dump

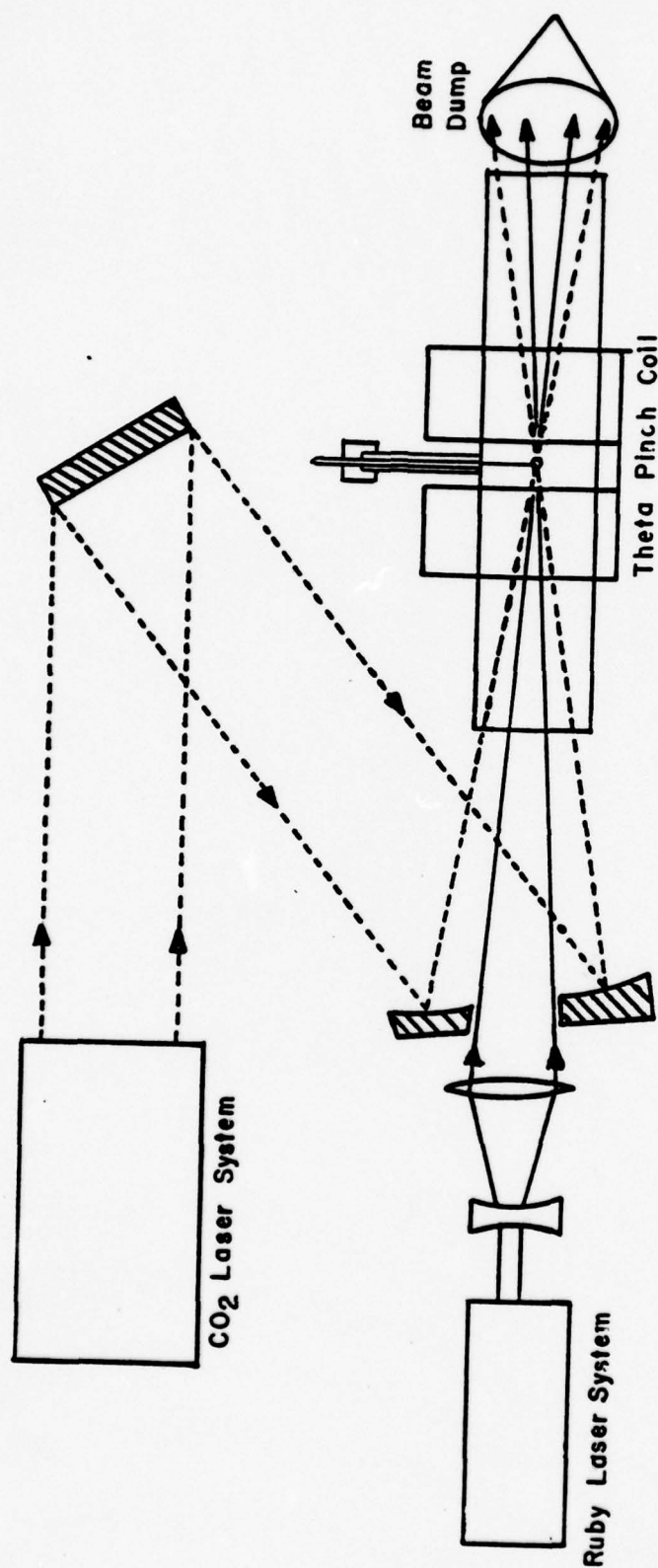Theta Pinch Coil

CO₂ Laser System

Ruby Laser System

Fig. III-10. Laser-Pellet-Plasma Interaction Scheme.

were doubly shielded with copper braid or solid copper
pipe all the way to a large screen room in which they
were recorded on oscilloscopes.

CHAPTER IV
EXPERIMENTAL RESULTS

Although it was not possible to complete all the investigations that were desirable, sufficient information was accumulated to satisfy the major goals of the research. The basic interaction mechanisms and resulting effects on the pellet targets have been observed and discussed. The ablation rates of the polystyrene spheres have been directly measured and plotted as a function of various plasma parameters. The feasibility of the sequential solid-plasma-laser interactions as a radiation source is considered with respect to the carbon line spectroscopy and streak camera observations. Much of the experimental results are presented in this chapter along with some description and analysis. The implications of these results are discussed further in the concluding chapter. As verified by Mach Zehnder interferometry, the average plasma density was not affected by local disturbances caused by the pellets. Similarly no corrections were made to account for the pellets' effect on the other average plasma parameters.

Ablation Rate Data

Experimental data showing a linear relationship be-
tween the left-hand-side (plasma parameters) and right-
hand-side (pellet parameters) of Eq. (II - 3) would be
sufficient to show the validity of the scaling law of
Parks and others.[11,15,16] This possibility was investi-
gated and the results are shown in Fig. IV-1. Previously
collected data on the plasma parameters (without pellets)
determined the four suitable filling pressures presented
in the figure. For these filling pressures $\bar{n}_e$ ranged
from 2.4 to 7.7×10^{22} m^{-3}, and $\bar{T}_e$ ranged from 108 to 126
eV. Typically r_{po} was between 50 and 150 μm while Δr_p
was between 1 and 6 μm. The dashed error bars represent
one standard deviation for all the collected pellet data
(up to ten pellets per filling pressure). The dashed
straight line was fitted to these data by a least squares
technique. The large horizontal error bars are due
chiefly to the errors in measuring the pellet diameters.
The solid error bars represent one standard deviation for
a reduced number of pellets (six per filling pressure)
after applying a statistical rejection technique known as
"Chauvenet's criterion"[53] in which observations, whose
deviation from the mean were greater than approximately
two standard deviations, were discarded completely. The
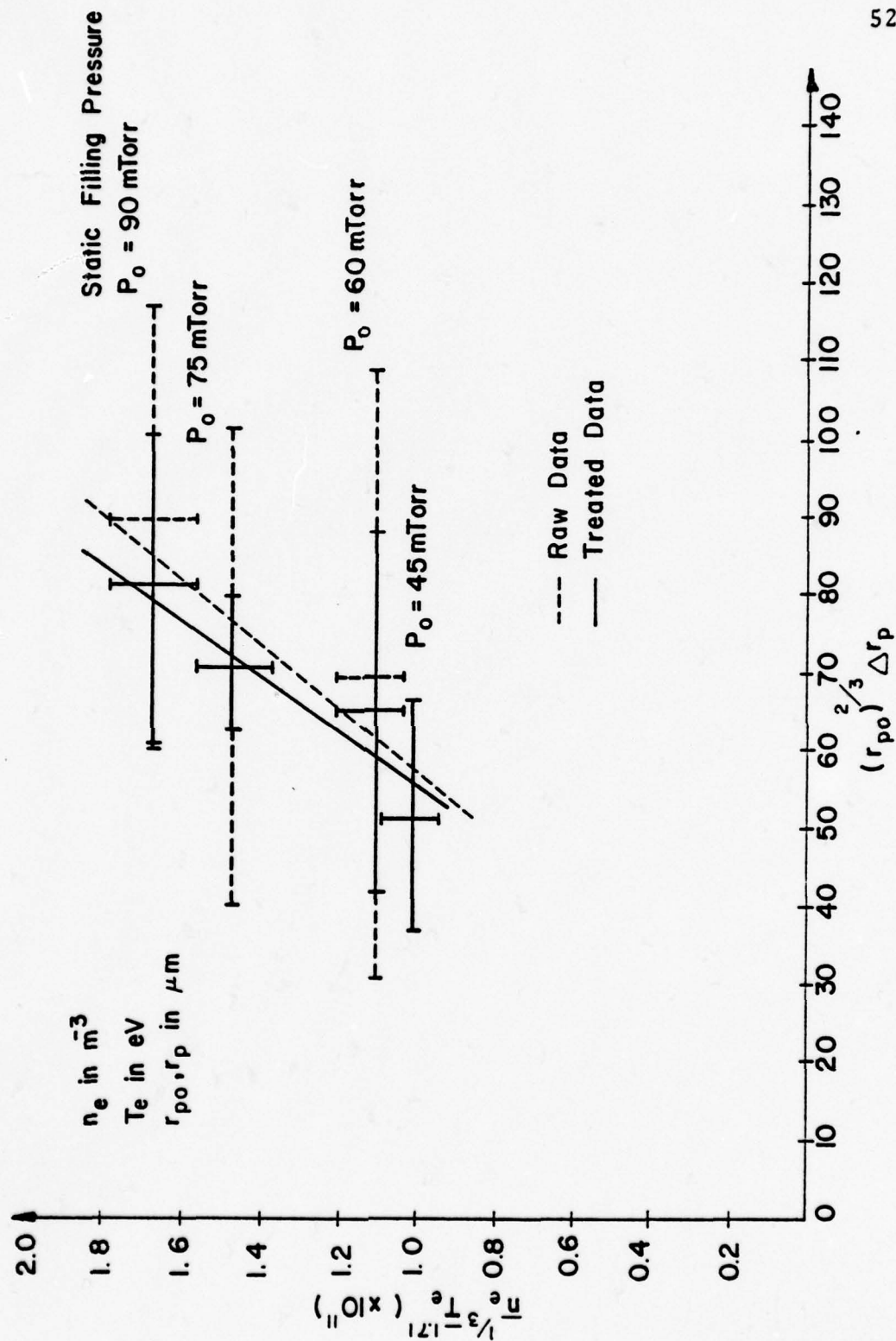tabulated data and an example application of the criterion

Fig. IV-1. Experimental Results in Terms of the Scaling Law Variables.

52

can be found in Appendix C. Again a least squares fit
was used to locate the solid straight line whose slope
can be used to determine the proportionality constant in
Eq. (II - 3). The average data do tend to support the
scaling theory, but the error bars are still too large to
draw any definite conclusions. Any further treatment of
the data would be unrealistic. Accumulating many more
data samples from the experiment would have been the best
way to improve the results.

Figure IV-2 presents some of the pellet data for two
filling pressures, plotting the reduction in radius
against the initial pellet radius. Since the interaction
time, Δt, is assumed to be a constant 2 μs for this
experiment, the vertical axis actually represents the
pellet surface regression speed, $\dot{r}_p$, or indirectly, the
ablation rate, given the density of a uniform polystyrene
sphere ($\doteq 1.05$ g/cm^3). The two straight lines were
fitted by a least squares method and are included only to
show the tendency for pellets exposed to higher initial
filling pressures to change more. As discussed earlier,
it is understood that $\dot{r}_p$ is not, in general, a linear
function of r_{po}, but it is approximately linear for this
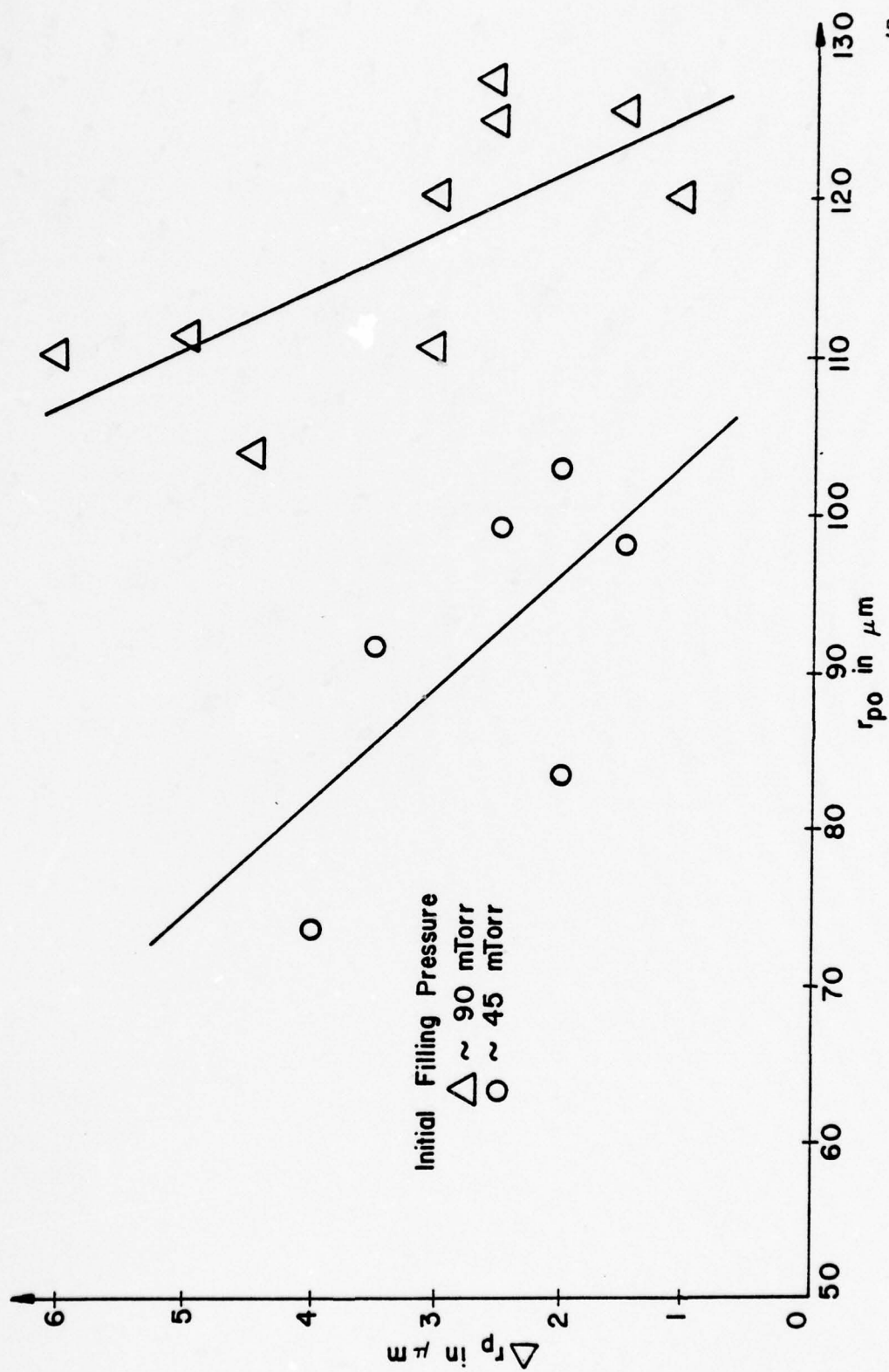small range of pellet parameters according to Eq.
(II - 3).

Fig. IV-2. Pellet Radius Reduction Versus Initial Pellet Radius.

54

The average plasma electron energy flux is plotted against what can be taken as the change in pellet volume in Fig. IV-3. Because of the relatively narrow range of plasma parameters, the data may be fitted to the linear solid line as shown. However, it is intuitively predictable and reasonable that this function is nonlinear and monotonically increasing, as indicated by the dashed line drawn through the mean values of the data. For instance, in order to ablate a greater volume of material from the surface, the energy flux must penetrate an ever increasing amount of the cloud material and overcome more losses in order to continue delivering energy to the surface. If the cloud provided no shielding, then the ratio of the energy incident upon the surface to the volume change of the pellet would be constant. Ablation data for hydrogen pellets have been reported at Riso,[54] but the results are so different, due to different pellet material and to their rotating plasma configuration that meaningful comparison is difficult.

Spectroscopic Results

By comparing the subsequent ionization stage intensities of carbon, the investigations revealed that at least the outer layers of the ablation cloud acquired temperatures between 2 and 6 eV, on time scales small
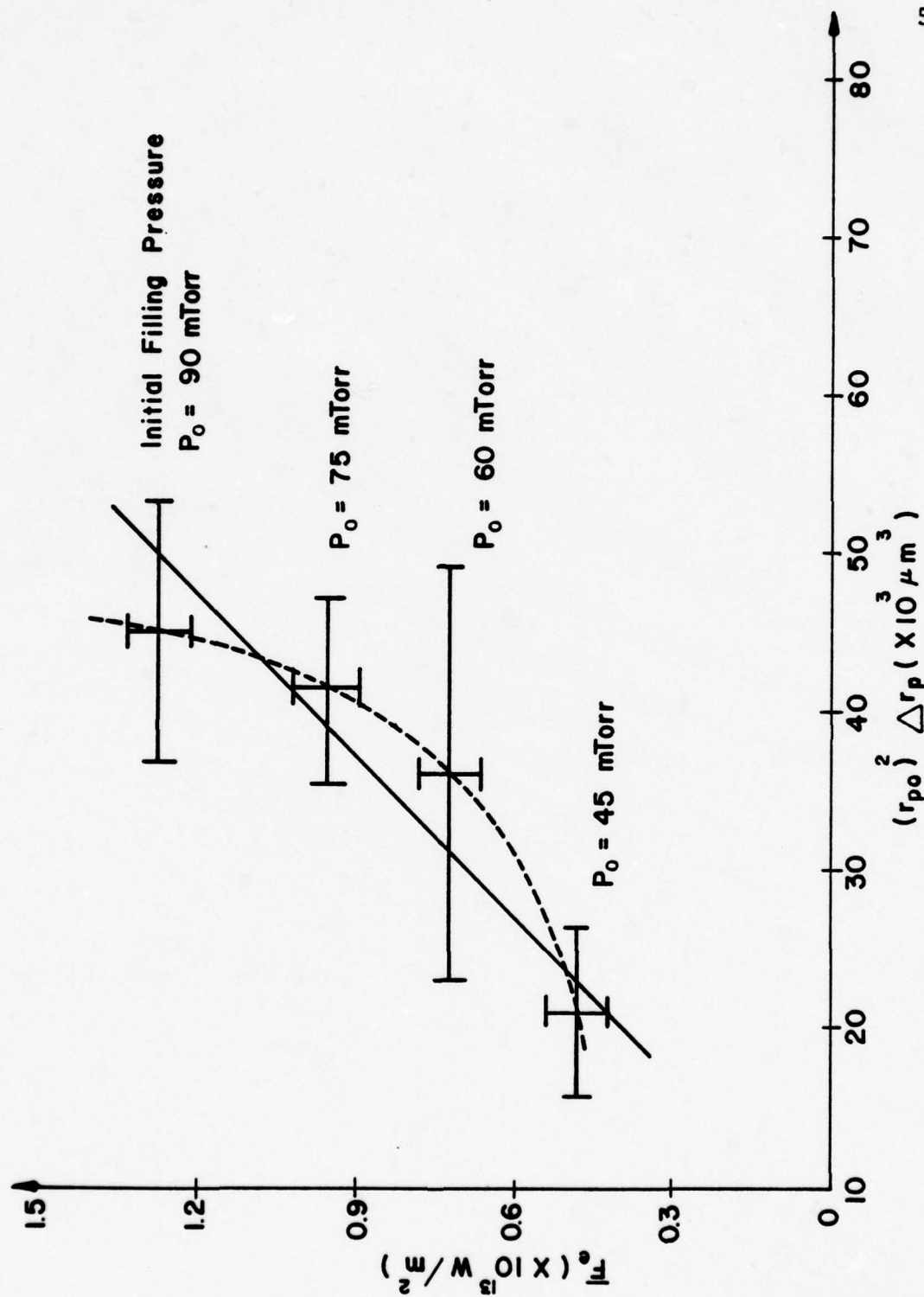
Fig. IV-3. Energy Flux Versus Volume Change.

56

with respect to the plasma-solid interaction time depending
upon the initial filling pressures and pellet sizes. For
typical controlled thermonuclear reactor (CTR) conditions
and for $r_{po} < .005$ m, the hydrogen pellet cloud is pre-
dicted to be, for the most part, ≤ 2 eV.[11] It was thus
assumed that it is the outermost cloud layers which pos-
sess these higher energies in this experiment since the
energy flux in this experiment is comparable to that of a
CTR plasma. No direct correlation could be made between
the line intensities and pellet sizes because the small
axial variation in the fixed pellet positions affected
the total intensity observed through the light pipe's
acceptance cone.

Figure IV-4 shows line drawings of three cases of
the observed carbon line, CIII (569.5 nm), at one filling
pressure, $P_o = 60$ mTorr. The plasma background or con-
tinuum near this wavelength is shown in part (a) of the
figure. The signal initially occurs about 400 ns after
triggering the rail gap switch, and the first few negative-
going peaks in region A correspond to the radial hydro-
magnetic oscillations (inertial bouncing) as the plasma
is being shock heated ahead of the rising magnetic field.
The large spike early in region B occurs at the beginning
of the second half-cycle, after the magnetic field (see
part (b)) has rung back through zero. As the plasma
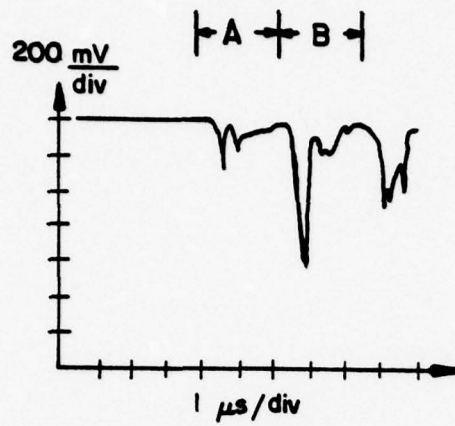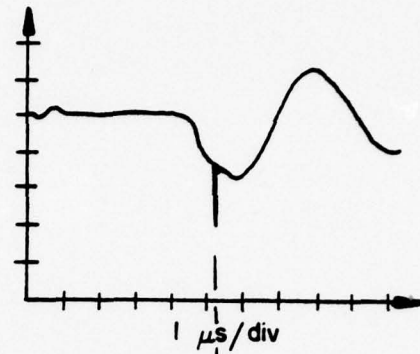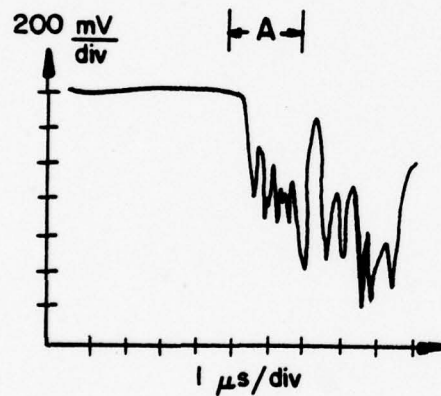
Fig. IV-4. CIII Line Intensities Versus Time for $P_0 = 60$ mTorr.

interacts with the vessel walls, carbon residue, and so
forth, it becomes dirty and cold and is no longer of
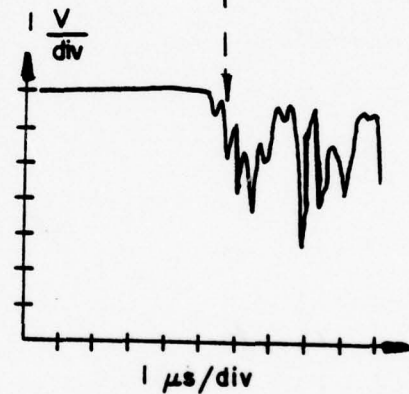interest for studying the pellet-plasma interaction.
Comparing part (a) with the case in which a pellet is
exposed to the plasma in part (c) makes it apparent that
there is considerable ionization throughout region A.

The addition of a 30 ns, 2.5 J pulse from the Q-
switched ruby laser focused on the pellet cloud produced
the effect shown in part (d) of Fig. IV-4. The laser
pulse timing monitor that is added to the B-field display
of part (b) shows, with a dashed line, the approximate
time the laser was discharged with respect to part (d).
Noting the different vertical scales of parts (c) and (d)
one can see that the amplitudes of the first peaks are
roughly the same, as they should be for similar experimen-
tal conditions. A considerable boost in the line inten-
sity is evident when the laser was fired and for some
time thereafter. It has already been reported[2] that the
increase and continuing intensity level indicates that
the plasma maintains the pellet cloud ionization and
continues to transfer energy more efficiently to the
cloud. This effect is probably due to a process in which
the laser effectively increases some of the collisional
cross sections involved in the solid-plasma interaction.
It is possible that the X-ray spectrum would be corre-

spondingly increased and sustained just as the visible
spectrum is affected.

Image Converter Camera Diagnostics

Examples of the streak camera photography are pre-
sented in Fig. IV-5. Parts (a), (b), and (c) all are the
results of initial filling pressure $P_O = 60$ mTorr, while
(d) occurred at $\doteq 10^{-6}$ Torr (no plasma). Part (a) shows
a typical pellet-plasma interaction that takes place be-
ginning with the first shock compression of the plasma
and continuing thereafter. In agreement with the carbon
line spectroscopy, the luminosity diminishes between the
radial density maximums until the third compression when
the vaporization of the surface and the ionization have
progressed to the point of sustaining the radiation.
Notice that the cloud diameter appears to be growing in
time, approaching one centimeter near the maximum com-
pression of the magnetic field.

For contrast, one can compare part (a) of Fig. IV-5
with part (b), which shows the result of the plasma alone
in a more compressed time scale. The streak duration and
exposure level are different than those of part (a) in
order to provide a direct comparison with the case of the
combination plasma-pellet-laser interaction of part (c).
The arrow points out the small bright spot that corresponds

(a) Plasma With Pellet.
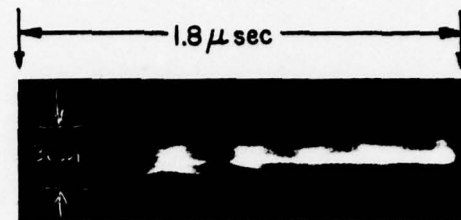
(b) Plasma Alone.
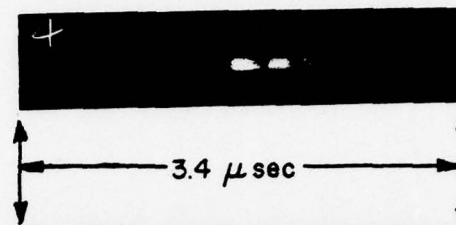
(c) Plasma, Pellet, and Ruby Laser.

(d) Vacuum, Pellet, and Ruby Laser.

Fig. IV-5. Image Converter Pictures of the Interactions

to the ruby laser pulse during the first shock compression. It is interesting how rapidly after the laser interaction the pellet cloud forms and expands. In fact, in about 300 ns it grows to the size that it took over 1.0 µs to form without the laser interaction. The quick formation and persistence was also seen in the spectroscopic results. This result was probably due, in part, to the breakup of the pellet into several smaller fragments, so that a many-particle cloud system with laser-enhanced ioniza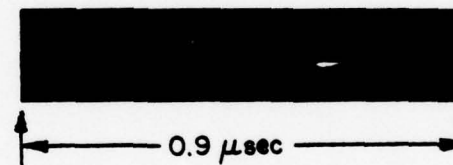tion is probably what was observed. All the pellets irradiated by the focused ruby laser (about 30 mJ delivered to one hemisphere), with or without a plasma, were broken apart so completely that none of the residue was recoverable for inspection. Streak camera photography of pellets exposed to the laser alone (Fig. IV-5, part (d)) showed the visible light from the interaction to be totally extinguished within about 50 ns. This agrees with the observation that, if the laser were fired "slightly" before the pellet-plasma interaction, essentially no difference could be observed in carbon line intensity or streak camera diagnostics when compared with the case of no laser at all. This observation seemed to be repeatable; hence, the pellet break-up either took longer than 1 µs, or it can be concluded that the increased surface area of the pellet alone had no

effect on the plasma-solid interaction.

Pellet Surface Effects

As indicated by the examples of Fig. IV-6, pellets hit by a partially focused laser (about 3 mJ delivered to one hemisphere) were pitted or burned in some asymmetric fashion, in contrast to the effect of the plasma alone.[55] The recovered pellets that were exposed to the plasma, alone appeared to be slightly elliptical. This result might be expected from an interaction with a cylindrical plasma that is radially pinched. The difference between the major and minor diameters was usually about two microns, just within the measurement capability. Examining the surface detail under a 13,000X magnification, a scanning electron beam microscope indicated that the pellets received a fine polish from the interaction with the plasma. Figure IV-7, part (a), is a photograph of a 253 μm diameter microsphere before exposure to the plasma, and part (b) represents the pellet's surface after interacting with a plasma of 60 mTorr filling pressure. The observed area is about 0.03% of the total pellet surface.

Only about 100 mJ of infrared energy from the CO_2 TEA laser could be deposited on the pellets in a vacuum. No visible or carbon line radiation was observed which

(a) "Large" Crater in Pellet.
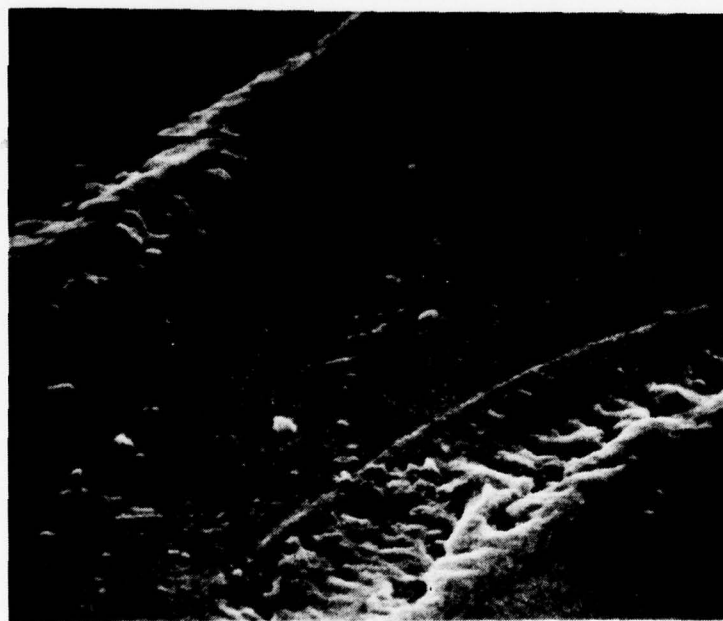
(b) A Pellet Surface Magnified 13,000x.

Fig. IV-6.   Examples of Low Intensity Laser Exposure.
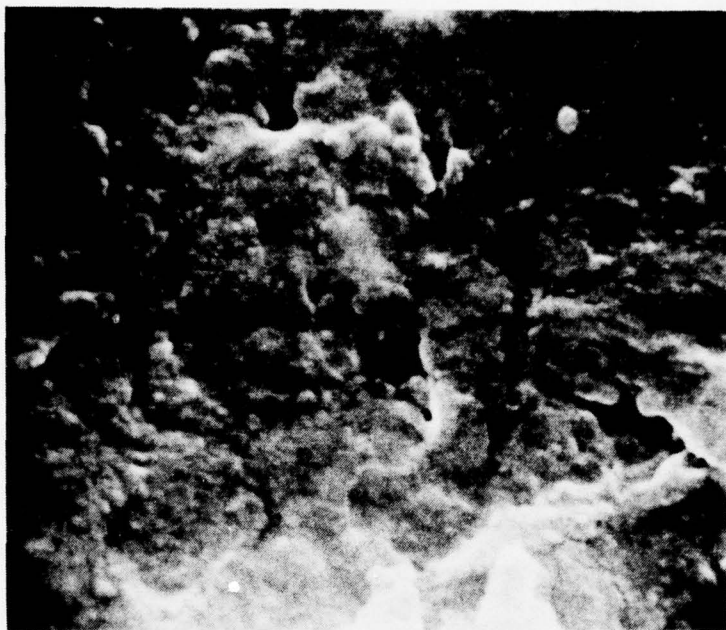
(a) Typical Pellet Surface Before Plasma Interaction.

(b) Plasma-polished Surface.

Fig. IV-7. Electron Microscope Photographs (13,000x Magnification).

implies that little or no ionization occurred. The only
observable effect on the pellet according to microscope
analysis was the occurrence of a cloudy or translucent
appearance. Even the supporting fiber was not broken
although it did appear to be deformed. Hence, an ionized
pellet cloud probably should be preformed before infrared
energy could be efficiently absorbed.

CHAPTER V

SUMMARY AND RECOMMENDATIONS

A continuation of the solid-plasma interaction studies originated by Nunnally[2] has produced data yielding ablation rate information for solid polystyrene pellets exposed to a theta pinch plasma. For the given plasma and pellet conditions, the averaged data lend support to the most recent ablation rate models and scaling laws. The large error bars that prevent detailed verification of the scaling laws could be reduced by taking more data and developing more accurate experimental measurement techniques. Other analytical models and computer simulation codes for pellet injection studies are being prepared and modified,[56,57] and hopefully these results can contribute to their verification and development.

In order to perform the detailed measurements required, it was necessary to work with the smallest, manageable microspheres available and to mount them in repeatable, fixed locations. Since the pellet motion is theoretically important only if T_e and n_e vary along its trajectory, a fixed pellet in a varying plasma is a good

67

simulation of a pellet being injected into a quasi-steady plasma. Any predicted anisotropic effects due to magnetic shielding of the pellets are not observable in a theta pinch as most of the magnetic field is excluded from the plasma. In addition to the previously discussed sources of error, one should include electrostatic shielding when the pellet surface acquires a static charge that interferes with the usual interactions. The only care taken concerning this effect was to treat all the microspheres identically such that the experimental results would be as repeatable as possible. Any unusual charge accumulation was easily noticed by the pellet's attraction to or repulsion from the glass surface while loading the pellet into the experiment. Obvious extensions of this work include acquiring the capability to handle and study smaller pellets and perhaps to introduce a high energy infrared laser beam in conjunction with the ruby prepulse for the purpose of heating the cold pellet plasma further.

On the basis of the discussion in Chapter II and the evidence obtained in this research, X-ray generation due to plasma-solid interactions alone appears far too inefficient to fulfill any economically practical application. Laser produced X-rays, on the other hand, can achieve high flux levels for very short durations. In

fact, a sufficiently large inertial-confinement laser
fusion device should produce, on a laboratory scale, many
of the radiation effects of nuclear weapons,[58] although
only for very short times. Evidence from carbon line
spectroscopy and streak camera photography suggests that
the generation of radiation in a plasma-pellet inter-
action is substantially enhanced and prolonged by the
addition of a short, low energy laser pulse. Hence, one
or several higher energy laser pulses used in combination
with a plasma-solid interaction should improve the yield
and make it possible to tailor the shape (in time) of the
generated radiation. To achieve relatively long duration
radiation pulses with reasonable efficiency and inten-
sity, it is therefore recommended that further studies be
directed toward the combined laser-plasma-solid inter-
action mechanisms. Extending the investigations to metal
pellets would also be desirable since it may enhance the
X-ray yield.

LIST OF REFERENCES

1. B. J. Eastlund and W. C. Gough, U.S. AEC, Report WASH-1132 (1969).

2. W. C. Nunnally, Technical Report No. 2 on Grant AFOSR-74-2639, Texas Tech University, Electrical Engr, Dept., Lubbock, Texas, 1974 (unpublished).

3. R. L. Nolen, Jr., L. B. Kook, and M. A. Ebner, Paper 5D7 at the 1977 IEEE International Conference on Plasma Science, RPI, Troy, New York (May 1977).

4. D. L. Musinski, T. M. Henderson, and R. J. Simms, Paper 5D8 at the 1977 IEEE International Conference on Plasma Science, RPI, Troy, New York (May 1977).

5. W. C. Nunnally, M. Kristiansen, and M. O. Hagler, Appl. Phys, Lett. <u>26</u>, 496 (1975).

6. L. Spitzer, Jr., <u>Physics of Fully Ionized Gases</u> (Interscience, New York, 1962), Chapt. 5.

7. D. J. Rose, Culham Laboratory Memorandum No. 82, 1968 (unpublished).

8. L. Spitzer, D. J. Grove, W. E. Johnson, L. Tunks, and W. F. Westendorp, USAEC Report NYO-6047, 1954 (unpublished).

9. S. L. Gralnick, Report No. 58, Plasma Laboratory, School of Engineering and Applied Science, Columbia University, New York, 1972 (unpublished).

10. S. Mitra, M. O. Hagler, and M. Kristiansen, Technical Mem. No. 1 on Contract AFOSR-69-1759, Texas Tech University, Electrical Engr. Dept., Lubbock, Texas, 1969 (unpublished).

11. P. B. Parks, Ph.D. Thesis, University of Illinois at Urbana-Champaign, Electrical Engr. Dept., Urbana, Illinois, 1977 (unpublished).

12. L. R. Peterson and A.E.S. Green, J. Phys. B $\underline{1}$, 1131 (1968).

13. W. T. Miles, R. Thompson, and A.E.S. Green, J. Appl. Phys. $\underline{43}$, 678 (1972).

14. P. B. Parks, Private Communication, University of Illinois at Urbana-Champaign, Electrical Engr. Dept., Urbana, Illinois.

15. D. F. Vaslow, IEEE Transactions on Plasma Science, $\underline{PS-5}$, No. 1, 12 (March 1977).

16. S. L. Milora and C. A. Foster, Technical Report ORNL/TM-5776, Oak Ridge National Laboratory, Oak Ridge, Tennessee (1977).

17. S. L. Gralnick, Nuclear Fusion $\underline{13}$, 703 (1973).

18. A. W. Cooper, Notes for the Short Course on Laser Aerodynamics, Air Force Weapons Laboratory, Kirtland AFB, N. M., April 11-22, 1977.

19. J. T. Schriempf, Technical Report NRL 7728, Naval Research Laboratory, Washington, D. C., (July 1974).

20. T. W. Johnston and J. M. Dawson, Phys. Fluids $\underline{16}$, 722 (1973).

21. J. M. Dawson and C. Oberman, Phys, Fluids $\underline{5}$, 517 (1962).

22. G. H. Canavan, P. E. Nielson, and R. D. Harris, AFWL Laser Digest LRD-72-1, Kirtland AFB, N. M. (June 1972).

23. Y. P. Raizer, Sov, Phys. JETP $\underline{21}$, 1009 (1965).

24. R. B. Hall, W. E. Maher, and R. S. P. Wei, Technical Report AFWL-TR-73-28, Air Force Weapons Laboratory, Kirtland AFB, N. M. (1973).

25. S. Byron, E. L. Klosterman, and R. B. Hall, J. Def. Res, $\underline{7B}$, 468 (1975).

26. D. E. Harrison, Naval Postgraduate School Report
    NPS 61-61Nb 75121.

27. B. Lax and A. H. Guenther, Appl. Phys, Lett. 21, 361
    (1972).

28. F. C. Jahoda, E. M. Little, W. E. Quinn, G. A. Sawyer,
    and T. F. Stratton, Phys. Rev. 119, 843 (1960).

29. W. M. Burton and R. Wilson, Proc. Phys. Soc. London
    78, 1416 (1961).

30. E. H. Beckner, Rev. Sci. Instrum. 38, 507 (1967).

31. T. C. Anestos and C. D. Hendricks, J. Appl. Phys. 45,
    1176 (1974).

32. R. A. Shatas, J. D. Settler, H. C. Meyer, and T. G.
    Roberts, J. Appl. Phys. 42, 5884 (1971).

33. J. W. Mather and P. J. Bottoms, Phys. Fluids 11, 611
    (1968).

34. N. J. Peacock, P. D. Wilcock, R. J. Speer, and
    P.D. Morgan in Proceedings of the 3rd IAEA
    Conference on Plasma Physics and Controlled
    Nuclear Fusion Research, Novosibirsk 2,
    51 (IAEA, Vienna, 1968).

35. H. Tawara, K. Ishii, and S. Morita, Nuclear Instrum.
    and Methods 132, 503 (1976).

36. K. O. Groeneveld, B. Kolb, J. Schader, and K. D.
    Sevier, Nuclear Instrum. and Methods 132,
    497 (1976).

37. H. S. Dunn and M. J. Lubin, MAS-TR-4 (Dept. of Mech.
    and Aerospace Science, College of Engr. and
    Appl. Science, University of Rochester, N. Y.,
    14627 (undated)).

38. S. Tamor, Final Report on Defense Nuclear Agency
    Contract DASA 01-71-C-0135 (October 1972).

39. M. Galanti and N. J. Peacock, 6th European Conference
    on Controlled Fusion and Plasma Physics,
    Moscow, USSR (1973).

40. J. L. Bobin, F. Floux, and G. Tonon in <u>Proceedings</u> <u>of the 4th IAEA Conference on Plasma Physics</u> <u>and Controlled Nuclear Fusion Research</u>, Madison <u>1</u>, 657 (1971).

41. J. A. McMordie and A. C. Simmons, J. Phys. D: Appl. Phys. <u>8</u>, L133 (1975).

42. B. C. Boland, F. E. Irons, and R. W. P. McWhirter, J. Phys. B (Proc. Phys. Soc.) <u>1</u>, 1180 (1968).

43. B. Lax, A. H. Guenther, D. R. Cohn, and W. Halverson in <u>Laser Interaction and Related Plasma</u> <u>Phenomena, Vol 3</u>, Edited by H. J. Schwarz and H. Hora, p. 859 (Plenum Publishing Corp., New York, 1974).

44. J. Nuckolls, L. Wood, A. Thiessen, and G. Zimmerman, <u>Digest of Technical Papers, VII International</u> <u>Quantum Electronics Conference, Montreal</u> (IEEE, New York, 1972).

45. P. J. Mallozzi, H. M. Epstein, R. G. Jung, D. C. Applebaum, W. J. Gallagher, R. E. Campbell, D. R. Grieser, and J. W. Beal, DNA 3922F, Final Report on Defense Nuclear Agency Contract DNA 001-74-C-0025 (February 1976).

46. P. J. Mallozzi, H. M. Epstein, R. G. Jung, D. C. Applebaum, B. P. Fairand, and W. J. Gallagher, ARPA Order Nr. 1723, Final Report on Advanced Research Projects Agency Contract DAAH01-71-C-0050, Vol. I and II (February 1972).

47. D. L. Smith, Technical Report No. 3 on Grant AFOSR-74-2639, Texas Tech University, Electrical Engr. Dept., Lubbock, Texas, 1975 (unpublished).

48. Technical Report AFWL-TR-65-1, Field Emission Corporation, McMinnville, Oregon (1966).

49. D. L. Smith, Plasma Laboratory Technical Memorandum AFOSR-74-2639-TM1, Texas Tech University, Elect. Engr. Dept., Lubbock, Texas, 1977 (unpublished).

50. H. R. Griem, <u>Plasma Spectroscopy</u>, (McGraw-Hill Book Co., New York, 1964), Ch. 6.

51. M. Martone and S. E. Segre, Plasma Phys. 13, 173
        (1971).

52. G. M. Molen, Technical Report, No. 3 on Grant AFOSR-
        69-1757H-3, Texas Tech University, Electrical
        Engr. Dept., Lubbock, Texas, 1973 (unpub-
        lished).

53. H. D. Young, Statistical Treatment of Experimental
        Data (McGraw-Hill Book Co., Inc., New York,
        1962) pp. 78-80.

54. L. W. Jorgensen, A. H. Sillesen, and F. Oster, Plasma
        Physics 17, 453 (1975).

55. S. Mercurio, Private Communication and Photographic
        Assistance, University of Wisconsin, Nuclear
        Engr. Dept., Madison, Wisconsin.

56. G. D. Kerbel, Private Communication, Oak Ridge
        National Laboratory, Oak Ridge, Tennessee.

57. C. E. Thomas, Jr., and P. A. Politzer, Private
        Communication, Massachusetts Institute of
        Technology, Cambridge, Mass.

58. C. M. Stickley, Comments in Laser Focus 13, 6 (1977).

APPENDIX

A.   An Analysis of Co-axial Pulse Transformers

B.   An Inexpensive High Voltage Probe

C.   Raw Ablation Data and an Example Application of
     Chauvenet's Criterion

APPENDIX A

AN ANALYSIS OF CO-AXIAL PULSE TRANSFORMERS*

by

R. Dollinger and D.L. Smith
Plasma Laboratory
Department of Electrical Engineering
Texas Tech University
Lubbock, Texas 79409

ABSTRACT

The basic idea of using a co-axial cable as an isolation pulse transformer for triggering spark gaps is not new.[1,2,3,4,5] However, there are several distinct advantages of driving the braid as the primary as opposed to driving the inner conductor. The fundamental advantage is that the ratio of the output voltage to the input voltage is unaffected by the thickness of insulation between the inner conductor(s) and the braid. Thus, the transformer with the braid as the primary works well for isolating high secondary to primary voltages. This and other advantages are demonstrated.

Introduction

Figure 1 shows the co-axial transformer being considered as a one turn loop of co-axial cable. Figure 1 also shows what is meant by the terminology of "driving the braid as the primary (Case I)" and "driving the inner conductor as the primary (Case II)." The relative advantages of Case I over Case II are discussed in this paper.

---

*This work was presented at the First IEEE Pulsed Power Conference, Lubbock, Texas, Nov. 9-11, 1976

Figure 2a shows the basic transformer circuit and Figs. 2b and 2c show the equivalent primary and secondary circuits, respectively. Of basic interest, is the voltage transfer ratio V_{out}/V_{in} when the trigger gap is open circuit (i.e. before the gap has broken down, $Z_{TG} = \infty$). It is desirable to have V_{out}/V_{in} as large as possible for reliable triggering. Table I gives the equations for the primary current $|I_p|$, the ratios of $|V_{out}/V_{in}|$ and $|\omega I_S/V_{in}|$, the normalized current in the trigger gap when the gap is short circuited (i.e. after the gap has broken down, $Z_{TG} = 0$).

The models in Fig. 2 are valid only for frequencies much less than the speed of light divided by the largest physical dimension of the transformer (i.e. the transformer must be much smaller than one wavelength). In actuality, the performance of the co-axial transmitter is not limited in this respect since transformers as large as a wavelength operate quite well. "Skin depth" effects, "proximity" effects and the electromagnetic radiation from the transformer acting as a magnetic dipole antenna have not been a problem.

Table II gives the parameters of some of the transformers tested and the values of $|\omega I_S/V_{in}|$, which are about the same for either case. The nomenclature used in the table is defined in Figs. 1, 2, and 3. From Fig. 4

it can be seen that V_{out}/V_{in} is independent of D_{Br}/D_{IC} for Case I but not for Case II. Thus, for Case I only, can one add as much insulation between the braid and the inner conductor as desired to isolate the secondary without affecting V_{out}/V_{in}. Hence, Case I works very well as a high voltage isolation transformer.

If one looks at a cross-section of one side of the transformer, it can intuitively be seen that all the flux generated by the current in the braid is external to the inner conductor. However, not all the flux generated by the current in the inner conductor is external to the braid (i.e. some of the generated flux is between the inner conductor and the braid). It is this difference that accounts for the results of Fig. 4. Theoretically, one can calculate (or use Ref. 6, p. 52) the inductance of a one turn loop with a major diameter D and a minor diameter D_{Br}. This inductance is equal to L_{Br} and equal to M because both inductances come from the same flux linkages. The inductance L_{IC} can be calculated for a one turn loop with a major diameter D and a minor diameter D_{IC}. Since D_{IC} is always less then D_{Br}, L_{IC} must always be greater than L_{Br}. The coefficient of coupling, k, can then be calculated from: $k = M/\sqrt{L_{Br}L_{IC}}$. These calculations agree quite well with the experimental data in Table II. The fact the $L_{IC} > M$ and that $M = L_{Br}$ accounts for the

differences between the two cases in Fig. 4. It should be noted that in Fig. 3b for Case I ($Z_{TG} = \infty$), that the output voltage across kL_S is V_{in} but the input voltage is only kV_{in} which is less than V_{in}. This "apparent" voltage step-up between kL_P and kL_S is the result of the perfect coupling between kL_P and kL_S. These arguments, of course, neglect the flux in this cross-section that is generated by the currents flowing in the remainder of the transformer.

Adding extra insulation between the braid and the inner conductor also decreases the capacitance "C" (see Fig. 3) between the braid and the inner conductor. It is desirable to have this "C" as small as possible as it is a source for unwanted common mode noise. Thus, if Case I is used (see Fig. 4), one can make "C" as small as necessary to reduce the common mode noise by adding extra insulation without affecting V_{out}/V_{in}, the performance of the transformer.

Figure 5 shows one transformer ($D_{Br}/D_{IC} = 21.3$) response to a square wave for Case I and Case II. One can see that for Case I, V_{out} is approximately V_{in}, but for Case II V_{out} is as indicated in Fig. 4. The "ringing" response of V_{out} has not caused problems in triggering spark gaps.

By "threading" one end of the inner conductor N times

through the braid, one can obtain a 1:N step-up trans-
former. In order to prevent the turn to turn capacitance
of the secondary from degrading the response, extra in-
sulation must be added between the turns to decrease this
capacitance. Neither the N secondary turns nor the extra
insulation between them has a noticeable affect on the
transformer coupling (i.e. $V_{out} = NV_{in}$ for $Z_{TG} = \infty$). The
experimental evidence of this is not shown here, but the
reasoning is the same as the explanation given for Fig. 4.

As an example, a 1:2 step-up transformer ($D \doteq 0.40$ m,
$D_{Br} \doteq 0.03$ m, $\ell \doteq 0.10$ m, inner insulation and conductor
of RG-8/U coaxial cable with extra insulation) is pres-
ently being used to provide a 300 kV, 30 ns risetime
trigger to a rail gap for the TeePee 1B Theta Pinch from
a 150 kV, 13 stage Marx bank. This step-up transformer
was needed (1) to provide the high voltage trigger pulse
required for reliable switching (2) to prevent damaging
the Marx bank modules by isolating them from a reverse
high energy common mode noise pulse of 75 kV when the
rail gap was fired and (3) to break a ground loop.

Acknowledgement

We thank Dr. J.P. Craig for his helpful suggestions.

References

1. Matick, R.E., Proc, of IEEE., 56, No. 1, p. 47, Jan. 1968.

2. Winningstad, C.N., I.R.E. Trans. on Nuc. Sci., 6, p. 26, March 5, 1959.

3. Ruthroff, C.L., Proc. of I.R.E., 47, p. 1337, Aug, 1959.

4. Harvey, R.J., Proc. of Symp. on Engr. Problems of Fusion Res., April 8-11, 1969, paper DII-10, Los Alamos Scientific Laboratory, Report LA-4250, Los Alamos, New Mexico 87544.

5. Boicourt, G.F., Clark, B.D., and Schofield, A.E., Private Communication, Los Alamos Scientific Laboratory, Los Alamos, New Mexico 87544.

6. Terman, F.E., Radio Engineers' Handbook (McGraw-Hill Book Co., New York and London, 1943).
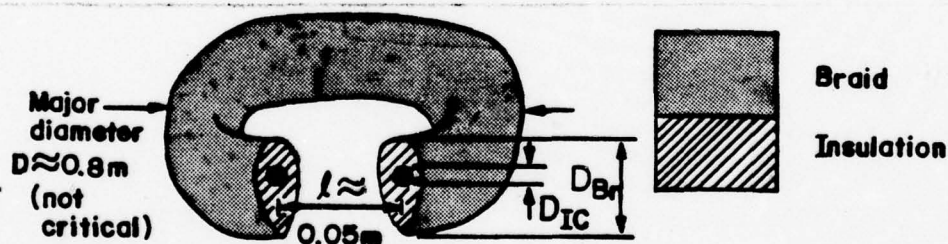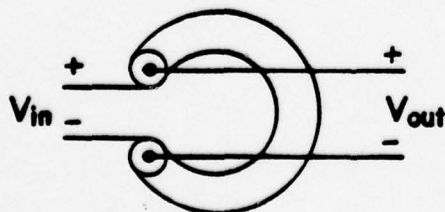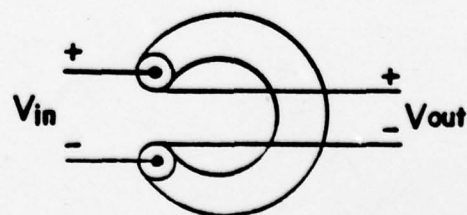
Fig. 1. Co-axial pulse transformer.
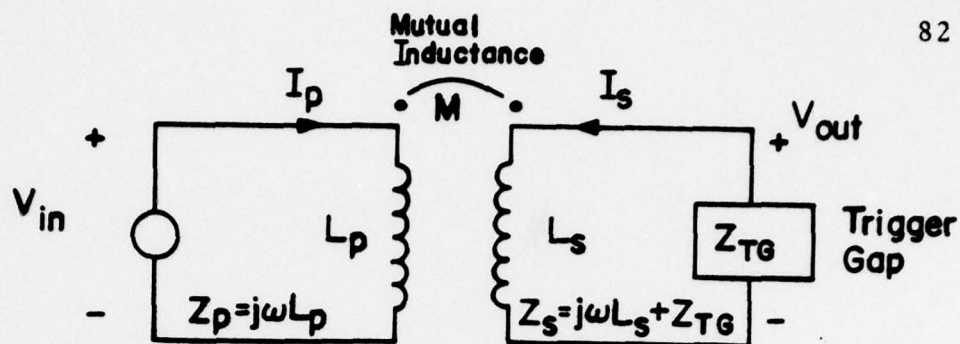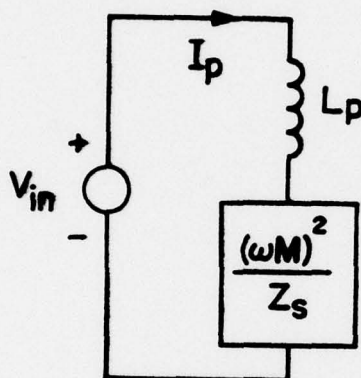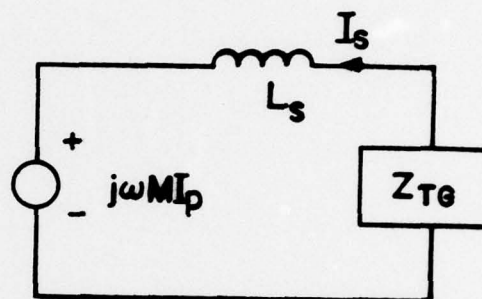
(a) Inductively coupled circuit.

(b) Equivalent primary circuit.   (C) Equivalent secondary circuit.

Fig. 2. Transformer circuit theory (Ref. 6, p149).

	$Z_{TG} = \infty$	$Z_{TG} = 0$
	Trigger gap has not broken down	Trigger gap has broken down
$|I_P|$	$V_{in}/\omega L_p$	$V_{in}/\omega(L_P - \frac{M^2}{L_S})$
$\left|\dfrac{V_{out}}{V_{in}}\right|$	M/L_p	0
$\left|\dfrac{\omega I_s}{V_{in}}\right|$	0	$M/(L_P - \frac{M^2}{L_S})$

Table I. Variables of interest.

Case I:
P→Br; S→IC
M=L_Br
Vout=Vin, Z_TG=∞

Case II:
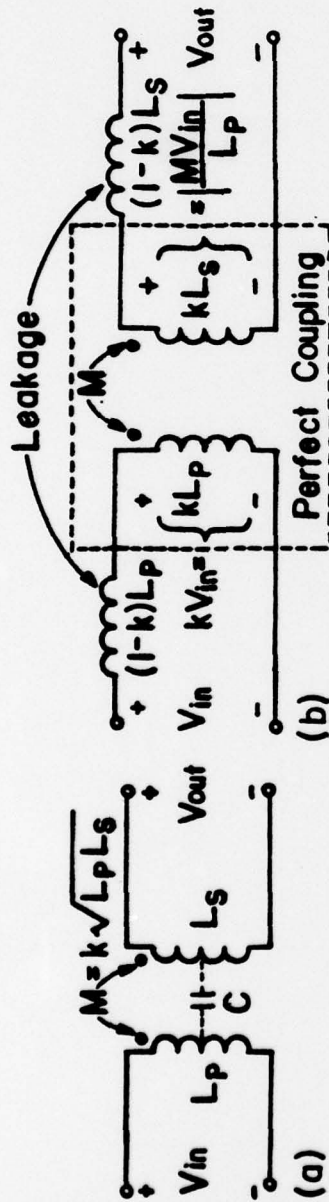P→IC; S→Br
L_IC > M=L_Br
Vout ≤ Vin Z_TG=∞

Fig. 3. Transformer circuits used in Table II. (Ref. 6, p151).

|	D_{Br}/D_{IC}	D_{Br} (cm)	$L_{Br}(\mu H)$ Braid Inductance (Total)	k	$M(\mu H)$ Mutual Inductance	$L_{IC}(\mu H)$ Inner Conductor Inductance	$\|\omega I_S/V_{in}\|$ for $Z_{TG}=0$		C(pf)
							Case I	Case II	
Single Turn Inner Conductor	1.33	2.14	2.10	0.950	2.07	2.25	4.41	1.33	≳310
	3.50	1.46	2.35	0.915	2.44	3.27	1.41	1.42	308
	6.35	1.46	2.34	0.847	2.45	3.59	1.03	1.03	218
	11.4	4.90	1.62	0.720	1.62	3.10	0.669	0.673	138
	21.3	4.90	1.65	0.688	1.65	3.50	1.17	0.225	122
Two Turns	3.50	1.46	2.35	0.873	4.70	12.4	0.654	0.667	308
	11.4	4.90	1.62	0.715	3.18	12.2	0.323	0.318	139

Table II. Measured transformer parameters.
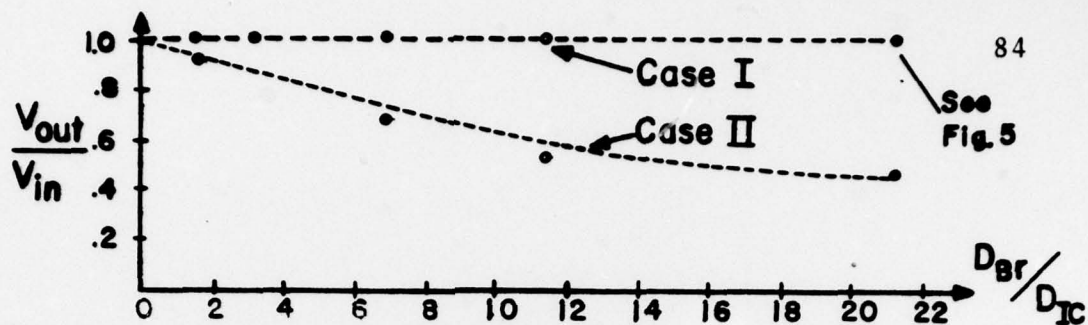
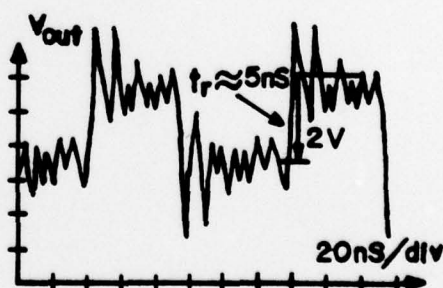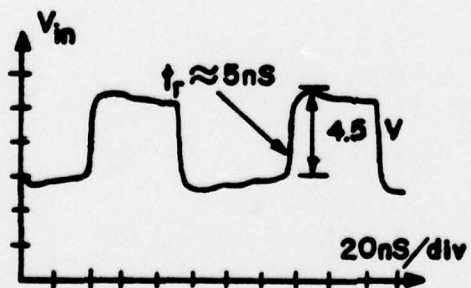Fig. 4. V_{out}/V_{in} (at 140 kHz) with $Z_{TG} = \infty$, 1:1 transformer.
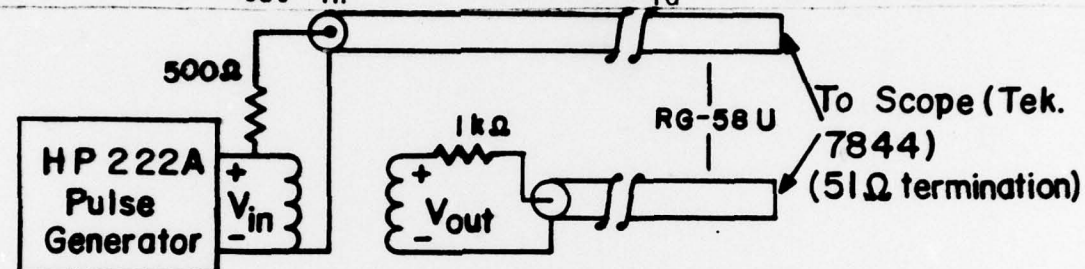
a) Test setup.

Case I
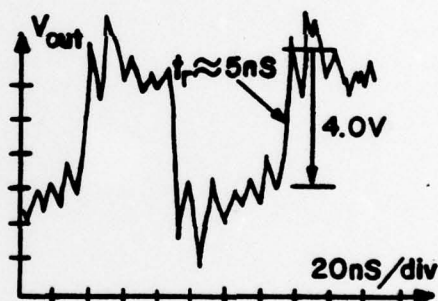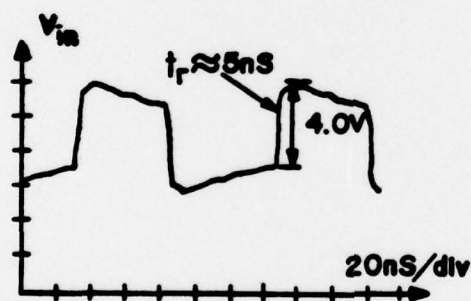
Case II

b) Typical results ($D_{Br}/D_{IC} = 21.3$).

Fig. 5. Co-axial pulse transformer response to square wave input.

APPENDIX B

AN INEXPENSIVE HIGH VOLTAGE PROBE*

by

R. Dollinger and D.L. Smith
Plasma Laboratories
Department of Electrical Engineering
P.O. Box 4439
Texas Tech University
Lubbock, Texas 79409

ABSTRACT

A simple, easily constructed, high voltage probe ($\leq$ 300 kV) with a good frequency response ($\leq$ 100 MHz) and high input impedance ($\geq$ 10 kΩ) is desirable in many applications. Such a probe, constructed of two concentric cylinders of "Velostat"[1] is reported.

Introduction

There are several well-known voltage divider techniques employed as high voltage probes. A capacitive and an inductive divider are shown in Fig. 1. Both suffer from high frequency ringing noise caused by the ever present stray reactances. They also place a reactive loading on the measured circuit that is often undesirable because the loading is frequency dependent. The more familiar resistive divider, as shown in Fig. 2, has a

---

*This work was presented at the First IEEE Pulsed Power Conference, Lubbock, Texas, Nov. 9-11, 1976.

limited frequency response because the signal may be shunted directly to ground by the stray capacitances and especially the variable stray capacitances. Decreasing the total chain resistance tends to improve the high frequency response; however, to prevent loading down the input circuit the total resistance should be as large as possible. Typical resistive dividers have a total resistance of $\leq$ 100 kΩ and a frequency response of $\leq$ 500 kHz.

The high frequency response can be improved by placing the resistive divider chain in a known electric field to decrease the effect of the variable stray capacitances. Two methods for doing this are shown in Fig. 3. A cylindrical metal housing for the chain, which is well sealed for shielding purposes, is not convenient to construct. Placing the chain between two large metal electrodes has the disadvantage that the electrodes must have a radius of curvature much larger than their separation distance. Thus, for a large voltage holdoff, the electrode size makes them necessarily expensive to construct and not very portable.

A method of providing a uniform electric field and graded stray capacitances around the resistive divider chain is by enclosing the high voltage chain inside a second resistive divider chain in a concentric cylindrical configuration. See Fig. 4a.[2] This allows the use

of electrodes similar to but much smaller than those of
Fig. 3b. The probe in Fig. 4a has an input impedance
$\geq$ 30 kΩ. It has a frequency response of $\geq$ 200 MHz and
can withstand voltage potentials of $\doteq$ 100 kV in air or
$\doteq$ 300 kV if immersed in oil. Although the probe works
very well, it has the disadvantages that the design re-
quires special order resistors (5 ea: 10 kΩ, 11J) with
a long delivery time and that its initial construction
is not simple, particularly because it is somewhat diffi-
cult to separate the oil and electrolyte and seal their
reservoirs without trapping or forming bubbles. This
compact arrangement is a big improvement over those of
Fig. 3, but the probe is still not light, especially when
immersed in oil. Finally, one is hesitant to measure the
unknown voltage of a high energy source for fear of ex-
ceeding the probe's high voltage or power rating and
damaging the unit.

We, therefore, have built and tested a probe of the
type shown in Fig. 4c, which has the distinct features of
being simple (3 man-hours to assemble and ½ hour to re-
pair) and inexpensive to construct, as well as, being
very light and portable. It typically has a good high
frequency response ($\leq$ 100 MHz) and is able to withstand
$\geq$ 300 kV without being immersed in oil. With a high input
impedance ($\geq$ 10 kΩ), it is a tool that would be very

useful in many research applications. The design of the probe is very similar to the one shown in Fig. 4a except that Velostat[1] replaces the inner resistor divider chain and the electrolyte. Velostat is a trade name for polyolefin plastic that is made conductive by the addition of carbon. No oil or electrolyte is used. Velostat film is available in 150 ft rolls of 4, 6, and 8 mil thicknesses and several widths (36-72 in). "Velostat layflat tubing" with 4 and 8 mil thicknesses and widths varying from 3 to 12 in can be purchased in 500 ft rolls. Solid rod stock has diameters from 1/8 to 13/16 in. Also, the top metal electrodes of Fig. 3c may be replaced by thin metal sheets since there are no oil or electrolyte reservoirs to seal. Even aluminum foil may be used for the electrodes; this allows their diameter, d_3, to be varied for fine tuning the probe response.

Table I contains a comparison of various sizes and styles of the new probe design. The parameters listed are the dimensions indicated in Fig. 4c plus the limiting risetimes (t_r) of the different styles. The response of two of these probe styles (f), $\leq$ 300 kV, and (g), $\leq$ 50 kV, is compared to a calibrated input signal in Fig. 5. The inner Velostat cylinder of probe (f) will dissipate $\geq$ 2 kJ of energy with only a 10% change in resistance ($\pm$10°C change).

References

1. "Velostat" - Trade name for polyolefin plastic that
    is made conductive by the addition of carbon.
    3M Co., Nuclar Products Dept., 3M Center,
    St. Paul, Minnesota 55101.

2. Henins, I., Progress Report No. LA-5656-PR, Los
    Alamos Scientific Laboratories, Los Alamos,
    New Mexico 87544, July, 1974.

if $Z \gtrsim 10 \dfrac{1}{C_2 \omega_{Min}}$

$V_{out} = \dfrac{1/C_2}{1/C_1 + 1/C_2}$

if $Z \gtrsim 10 \, \omega_{Max} L_2$

$V_{out} = \dfrac{L_2}{L_1 + L_2}$
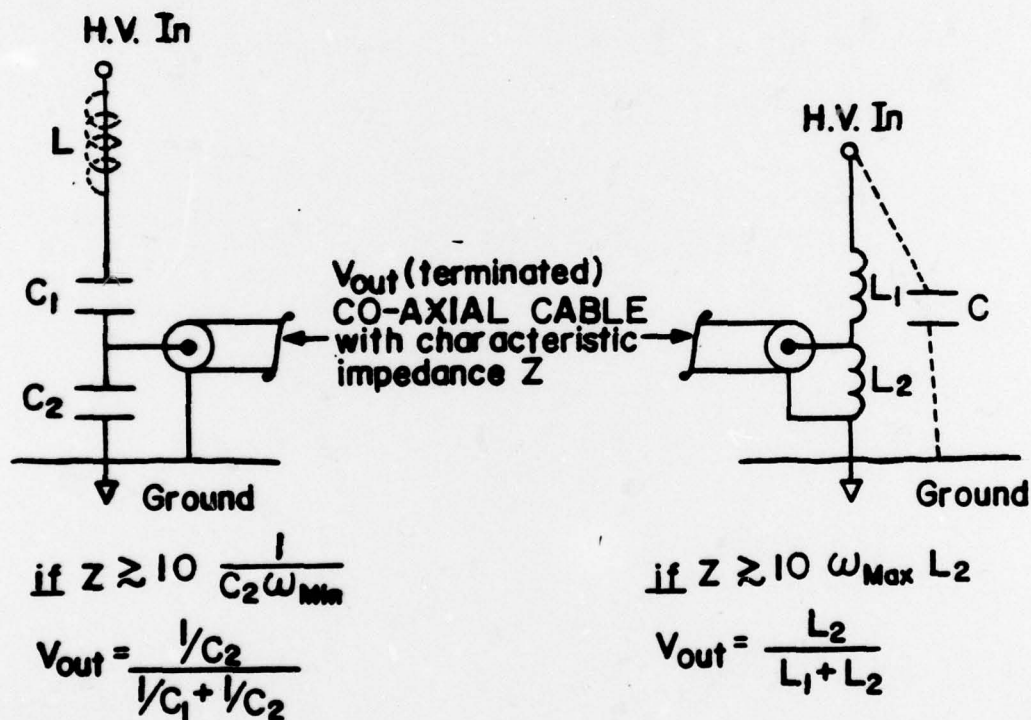
Fig. 1. Capacitive and inductive voltage divider chains.
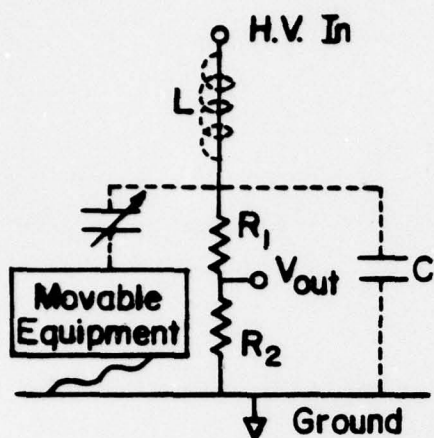
Fig. 2. Resistive divider chain.

(a)

(b)
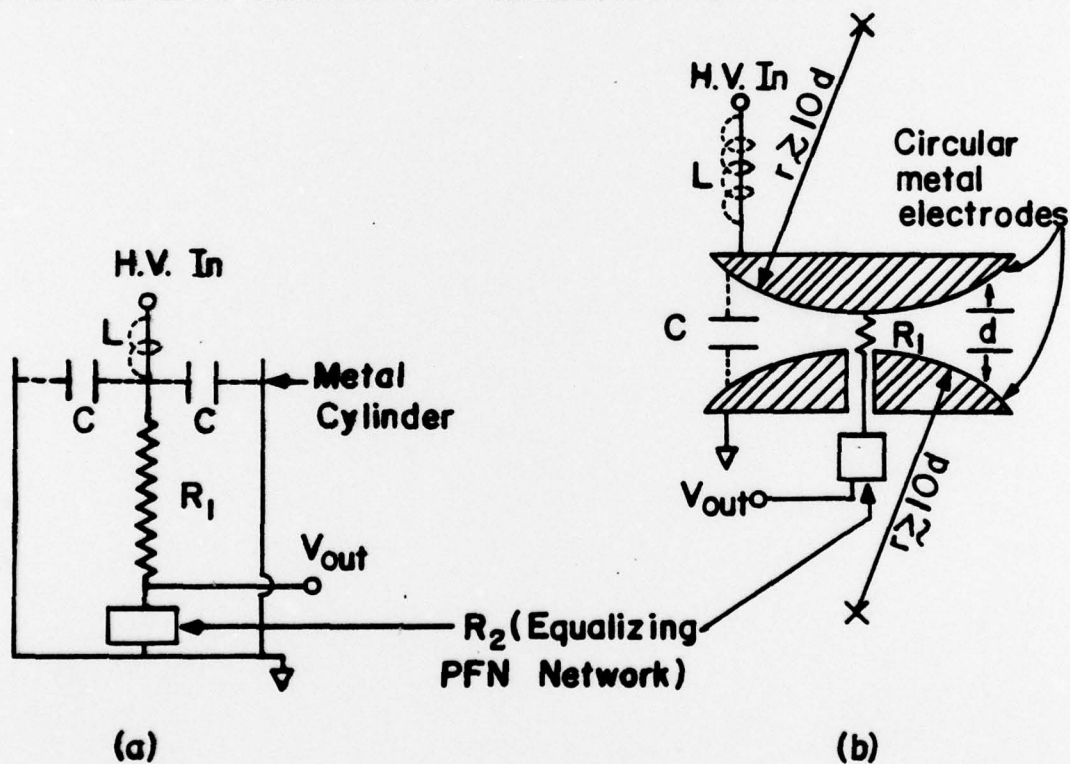
Fig. 3. Two methods of removing the variable capacitance in Fig. 2.

d_3

d_2

d_1

R_1

Air

Air

Air

R_1

Circular Thin Metal Sheet

ℓ

Velostat* Rod, or Velostat* sheet film on an insulating cylinder for support, or Velostat* tubing.
*Trade Name for Polyolefin plastic made conductive with carbon. 3 M Co., Nuclear Products Dept.[1]

(c) High Voltage Probe made with Velostat.*

R_1

CO—AXIAL CABLE with characteristic impedance Z
(Terminated)

$$V_{out} = \frac{Z}{Z + R_1}$$

(b) Model of a. and b.

R_1

0.18 m
0.07 m
0.04 m
0.014 m

0.05m

0.05 m

0.215m

drain hole

Concentric Insulating Cylinders

OIL

ELECTROLYTE

CIRCULAR METAL ELECTRODE

(a) L.A.S.L High Voltage Probe[2]

Fig. 4. Preferred methods for HV probe design.

Approximate Dimensions		$d_1(m)$	$d_2(m)$	$d_3(m)$	$\ell(m)$	Risetime t_r
H.V. Probe made with 8 mil Velostat[1] film ($\frac{V_{in}}{V_{out}} \approx 1,500:1 \rightarrow 3,000:1$)	(a)	0.089	none	none	1.	$\gtrsim 3\mu S$
	(b)	0.089	0.091	none	1.	$\gtrsim 300nS$
	(c)	0.089	0.091	~ 0.5	1.	$\gtrsim 200nS$
	(d)	0.027	0.089	0.089	1.	$\gtrsim 100nS$
	(e)	0.027	0.089	~ 0.5	1.	$\gtrsim 50nS$
	(f)	0.027	0.16	~ 0.5	1.	$\gtrsim 20nS$
	(g)	0.007	0.06	0.06	0.2	$\gtrsim 10nS$
L.A.S.L. H.V. Probe[2] ($\frac{V_{in}}{V_{out}} \approx 1,000:1 \rightarrow 2000:1$)		0.008	~ 0.035	0.18	0.215	$\lesssim 10nS$

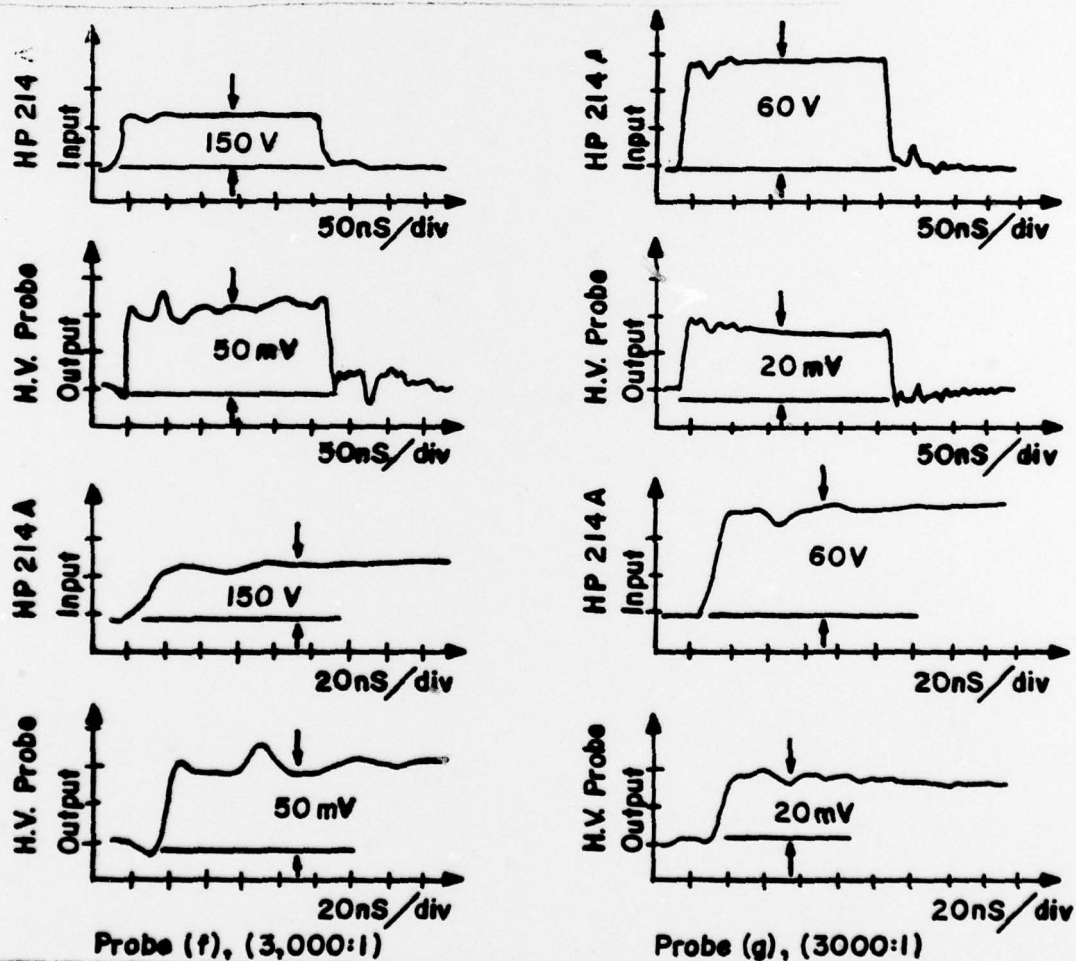Table I. Comparison of different probe styles.

Fig. 5. Probe response to a calibrated input signal.

APPENDIX C

RAW ABLATION DATA AND AN EXAMPLE APPLICATION

OF CHAUVENET'S CRITERION

The raw ablation rate data acquired from microscope
measurements of the change in radius of the pellets,
exposed to the plasma only, are tabulated on the fol-
lowing page. The x_1 values represent the product,
$(r_{po})^{2/3} \Delta r_p$, from Eq. (II - 3) where r_{po} and Δr_p are
both in microns. The average error in x_1, ± 4, comes from
an individual measurement error of ± 0.25 μm which was
usually averaged over about four measurements.

According to Chauvenet's criterion,[1] an observation
should be discarded if its deviation from the mean is so
large that the probability of occurrence of a deviation
that large or larger is less than 1/20. If this cri-
terion is observed, one may eliminate completely any
measurement whose deviation from the mean is approxi-
mately 1.96σ or larger. To illustrate an application of
this technique, consider the case for which the initial
filling pressure was 75 mTorr. The number of observa-
tions, their mean, and the standard deviation from the
mean can be readily found as follows:

Raw Ablation Rate Data from Microscope Measurements

P_o(mTorr):	90			75		
r_{po}	Δr_p	$x_1(\pm 4)$		r_{pc}	Δr_p	$x_1(\pm 4)$
124.5	2.5	62.4		115.0	1.0	<u>23.6</u>
127.0	2.5	63.3		118.0	2.5	60.1
110.5	3.0	69.1		123.5	2.5	62.0
120.0	3.0	73.0		111.0	3.0	69.3
104.0	4.5	99.8		117.5	3.0	72.0
111.0	5.0	11		121.0	3.0	73.4
110.0	6.0	<u>138</u>		122.0	3.5	86.1
				138.0	4.5	<u>120</u>

P_o(mTorr):	60			45		
r_{po}	Δr_p	$x_1(\pm 4)$		r_{po}	Δr_p	$x_1(\pm 4)$
110.0	1.0	<u>23.0</u>		98.0	1.5	31.9
115.0	1.0	<u>23.7</u>		84.0	2.0	38.4
130.0	1.5	38.5		103.5	2.0	44.1
93.0	2.0	41.0		99.0	2.5	53.6
119.5	2.5	60.8		74.0	4.0	70.6
125.0	2.5	62.5		92.0	3.5	71.3
101.5	3.0	65.5				
95.5	3.5	73.3				
106.5	3.5	78.5				
114.5	4.5	106				
124.5	5.0	<u>125</u>				
122.0	5.5	<u>135</u>				

$$n_0 = 8$$

$$\overline{x}_0 = (\sum_i x_i)/n_0 \doteq 70.8$$

$$\sigma_0 = ((\sum_i x_i^2/n_0) - (\overline{x}_0)^2)^{\frac{1}{2}} \doteq 25.2 \ .$$

Since two values of x_i, 23.6 and 120, fall very near to $1.96\sigma_0$, their probability of occurrence is about 1/20, and they may be discarded. This reduced the number of observations by two, and the mean and standard deviation may be recomputed.

$$n_1 = 6$$

$$\overline{x}_1 = (\sum_i x_i)/n_1 \doteq 70.5$$

$$\sigma_1 = ((\sum_i x_i^2/n_1) - (\overline{x}_1)^2)^{\frac{1}{2}} \doteq 8.3$$

This is a significant improvement in the size of the standard deviation, but the criterion cannot be taken for granted. To apply it more than once would result in the loss of important data and should never be considered.

All the underscored values in the tabulated data were eliminated by applying Chauvenet's criterion to

produce the reduced error bars on Fig. IV-1. Other more complicated data rejection techniques do exist, but they would be impractical to try to apply to such relatively small quantitites of data.

Reference

1. Young, H.D., Statistical Treatment of Experimental Data (Mc Graw-Hill Book Co., Inc., New York, 1962) pp. 78-80.